An energy preserving time scheme based on the mortar element method for effective transmission conditions between fluid and solid domains in transient wave propagation problems

Alexandre Imperiale

▶ **To cite this version:**

Alexandre Imperiale. An energy preserving time scheme based on the mortar element method for effective transmission conditions between fluid and solid domains in transient wave propagation problems. International Journal for Numerical Methods in Engineering, 2023, 124 (14), pp.3250-3273. 10.1002/nme.7246 . cea-04134551

HAL Id: cea-04134551
https://cea.hal.science/cea-04134551

Submitted on 20 Jun 2023

HAL is a multi-disciplinary open access archive for the deposit and dissemination of scientific research documents, whether they are published or not. The documents may come from teaching and research institutions in France or abroad, or from public or private research centers.

L'archive ouverte pluridisciplinaire **HAL**, est destinée au dépôt et à la diffusion de documents scientifiques de niveau recherche, publiés ou non, émanant des établissements d'enseignement et de recherche français ou étrangers, des laboratoires publics ou privés.

An energy preserving time scheme based on the mortar element method for effective transmission conditions between fluid and solid domains in transient wave propagation problems

Alexandre Imperiale[a,*]

[a] *Université Paris-Saclay, CEA, List, F-91120, Palaiseau, France*

Abstract

We are interested in providing an efficient numerical scheme to represent wave propagation in time domain for configurations where a fluid domain and a solid domain are separated by a thin coating layer. Various computational challenges and bottlenecks occur in this context: incorporating fluid – solid coupling, enabling non-conform space discretization when wavelengths greatly differ from the fluid and the solid domain, and rendering robust time discretization *w.r.t.* the thin layer thickness. In order to address these issues, the proposed approach combines the mortar element method with so-called effective transmission conditions, where the effect of the coating layer is incorporated through spring – mass coefficients at the interface between the fluid and solid domain. Using discrete energy arguments, we are able to prove that the associated fully discrete scheme is stable upon a stability condition independent of the thin coating layer. Moreover, we provide an efficient time marching algorithm leading to significantly improved performances, illustrated in 2D and 3D configurations linked to ultrasonic testing experiments modeling.

Keywords: acoustics; time integration, explicit; finite element methods;

1. Introduction

In industrial applications, assessing structure integrity is an important aspect of safety requirements, and is often performed using Ultrasonic Testing (UT) methods. They rely on the interaction between high-frequency waves and potential flaws or material inhomogeneities. Insuring the reliability of a UT method is a challenging task and may require modeling and simulation. We consider the problem of efficient numerical modeling of high-frequency transient wave propagation in a configuration where a solid material is surrounded by a fluid, and at the fluid – solid interface a thin layer of different material is present. The thickness of this layer, denoted by η in the following, is assumed to be small compared to the minimal wavelength of interest $\lambda_{\min}$, leading to an asymptotic adimensional parameter $\eta/\lambda_{\min} \ll 1$. This configuration typically occur when simulating UT of immersed coated specimens. The computational challenges associated to this type of configurations are threefold:

- The thickness of the coating material degrades the efficiency of standard approaches based on explicit time schemes, as they suffer from a stability condition on the time step in $O(\eta)$.
- The wavelength in the fluid are usually smaller than in the solid (due to lower wave speed). Hence traditional conform approaches will impose an over-refined mesh in the solid domain, leading to a potentially significant cost overhead.

*Corresponding author
Email address: alexandre.imperiale@cea.fr (Alexandre Imperiale)

– As any fluid – solid coupling problem, one has to operate a specific treatment in order to incorporate the normal stress and normal velocity continuity conditions within their numerical scheme.

Various tools and techniques can be found in the literature to overcome some of these computational bottlenecks. For instance, authors in [1, 2] use an implicit scheme dedicated to the thin layer. Their approach alleviates the dependency of the timestep *w.r.t.* the layer thickness. It is based on the mortar element method [3, 4, 5] allowing for non-conform coupling between the domains. However it is done at the price of solving at each iteration a linear system of size proportionate to the number of Degrees of Freedom (DoFs) in the layer and would require some adjustments to incorporate fluid – solid transmission conditions. In [6, 7] a local time stepping method is proposed which effectively reduces the influence of refined or complex regions of the mesh onto the stability condition of the explicit time scheme. This is performed by adding sub-iterations between coarse time steps. Their approach imposes the use of Discontinuous Galerkin (DG) methods [8] in order to address non-conform meshes, and cannot support as-is coupling between fluid and solid propagators. Other approaches rely on building effective wave propagators in the coating layer based upon asymptotic developments – the asymptotic parameter being the ratio $\eta/\lambda_{\min}$. A typical example in the literature is [9, 10, 11]. Recently authors in [12] derive effective transmission conditions (ETC) between two solid domains surrounding the layer while insuring convergence to the exact solution as the thickness tends to zero. Their effective numerical procedure leads to a time step independent of the layer thickness, however supporting acoustic – elastic waves coupling with non-conforming meshes is not addressed by their approach.

Inspired by this seminal body of work, our approach combine the use of ETC – as in [9] – with an adequate form of the mortar element method – as in [1, 2]. It is in essence the extension of [11] to configurations with fluid and solid propagators. For these volume propagators, even though we believe that our approach could apply to more recent space discretization procedures, *e.g.* DG methods, we consider exclusively conform spectral finite elements [13]. The simplicity and performances of this approach still makes it a landmark for efficient numerical wave propagation modelling, and is present in various legacy codes [14, 15, 16]. The mortar unknowns are treated with an implicit time-scheme so that the stability condition of the overall numerical procedure is independent of the layer thickness and its effective parameters. This method supports (by construction) non-conform meshes, and we are able to adapt it to support fluid – solid coupling. Combining these elements we address the various computational challenges associated to the configurations of interest.

The outline of our paper is as follows. In Section 2 we detail the modeling setting used to represent UT experiments of an immersed and coated solid material. In Section 3 we present the numerical procedure leading to a fully discrete scheme. This procedure combines spectral finite elements [13] for the space discretization and second order schemes [17] for the time discretization. In this section we also analyze – using a discrete energy conservation property – the condition on the time step for the fully discrete scheme to be stable, and we provide an efficient time-marching algorithm. We illustrate our approach in Section 4 with some numerical results in 2D and 3D, and provide some conclusions and perspectives in the last section.

2. Wave propagation through an immersed and coated solid

2.1. Geometrical considerations

Let $N = 2$ or $N = 3$ denotes the space dimension. As depicted in Figure 1, we consider the open domain $\Omega_{\rm s} \subset \mathbb{R}^N$ occupied by a solid material subject to an UT experiment. This solid material is partially adjacent to a fluid (typically water) occupying the fluid domain $\Omega_{\rm f}$. Between the solid and fluid domains, we consider a thin coating material occupying the volume Ω^η, where η represents an upper bound of the (local) thickness of the coating domain. As a basic assumption of the following developments, we assume that η is significantly smaller than the minimal wavelength of interest $\lambda_{\min}$, justifying the name "coating" domain.

Additionally, we consider an extruded structure of Ω^η that we detail in this subsection in a 2D context for simplicity – the extension for $N = 3$ being conceptually straightforward. Let Γ represents the "middle" line of the domain characterized by its parametric coordinate transformation $\boldsymbol{\psi} : [0; 1] \mapsto \mathbf{x} \in \Gamma$, assumed

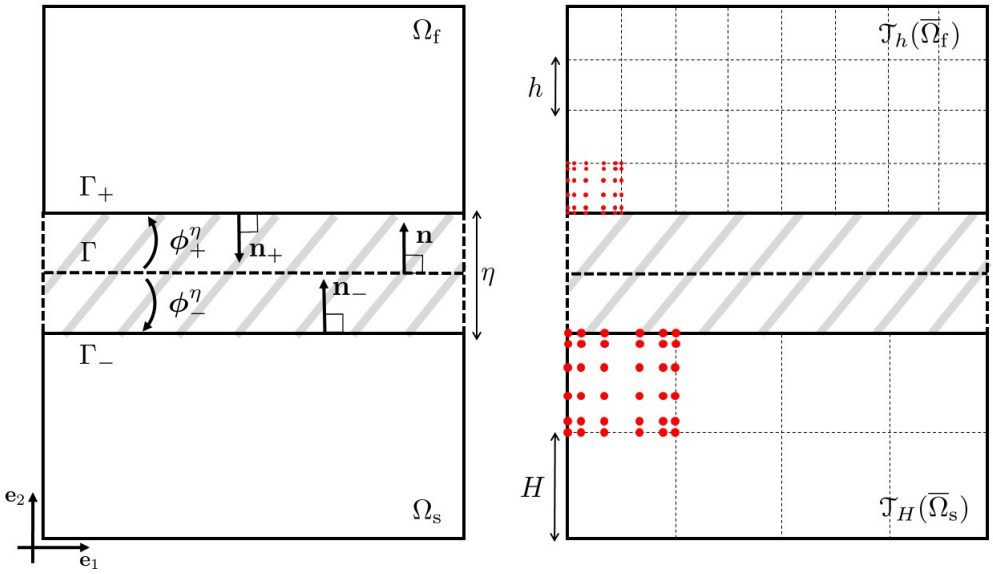

Figure 1: (Left) Representation of the type of geometrical configuration of interest for $N = 2$. The hatched area between the solid domain Ω_s and the fluid domain Ω_f represents the coating layer Ω^η. (Right) Schematic of the different discretization parameters used for the fluid and solid domains. Here the solid mesh step H is twice the fluid mesh step h. The order is $p = 5$, and the red dots are the Gauss-Lobatto nodes defining the local Lagrange polynomials.

to be a $\mathcal{C}^1$ – diffeomorphism. Let $\Gamma_\pm$ be the "upper" and "lower" boundary lines of the domain. They are obtained from the middle line through the transformations $\boldsymbol{\phi}_\pm^\eta : \mathbf{x} \mapsto \mathbf{x}' \in \Gamma_\pm$, *i.e.*

$$\Gamma_\pm = \Big\{ \mathbf{x}' \;\Big|\; \mathbf{x}' = \boldsymbol{\phi}_\pm^\eta\big(\boldsymbol{\psi}(u)\big), \quad \forall u \in [0;1] \Big\}.$$

These transformations depend on the upper bound of the thickness η and are also assumed to be $\mathcal{C}^1$ – diffeomorphisms. The remaining "left" and "right" boundary lines of the domain denoted by Γ_0 and Γ_1 are segments defined as

$$\forall \beta \in \{0,1\}, \quad \Gamma_\beta = \Big\{ \mathbf{x}' \;\Big|\; \mathbf{x}' = v\boldsymbol{\phi}_+^\eta\big(\boldsymbol{\psi}(\beta)\big) + (1-v)\boldsymbol{\phi}_-^\eta\big(\boldsymbol{\psi}(\beta)\big), \quad \forall v \in [0;1] \Big\},$$

and we define the domain Ω^η as the open set admitting as boundary $\partial\Omega^\eta = \Gamma_+ \cup \Gamma_- \cup \Gamma_0 \cup \Gamma_1$. In the following we assume that $\Gamma_\pm$ are translations of Γ, *i.e.*

$$\forall \mathbf{x} \in \Gamma \qquad \boldsymbol{\phi}_\pm^\eta(\mathbf{x}) = \mathbf{x} \pm \tfrac{\eta}{2}\mathbf{e}_2, \tag{1}$$

see Figure 1 for a representation of such configurations. Upon this assumption we have the following straightforward result.

Lemma 1. *Let* $\mathbf{n}$ *be the unitary normal vector field of* Γ *oriented from* Γ_- *to* Γ_+*, and* $\mathbf{n}_\pm$ *be the unitary normal vector fields of* $\Gamma_\pm$ *outgoing from* Ω_f *and* Ω_s *respectively. For any vector fields* $\mathbf{f} \in [L^2(\Gamma_+)]^N$ *and* $\mathbf{g} \in [L^2(\Gamma_-)]^N$ *we have*

$$\int_{\Gamma_+} \mathbf{f}\cdot\mathbf{n}_+ \,\mathrm{d}\Gamma_+ = -\int_\Gamma (\mathbf{f}\circ\boldsymbol{\phi}_+^\eta)\cdot\mathbf{n}\,\mathrm{d}\Gamma, \qquad \int_{\Gamma_-} \mathbf{g}\cdot\mathbf{n}_- \,\mathrm{d}\Gamma_- = \int_\Gamma (\mathbf{g}\circ\boldsymbol{\phi}_-^\eta)\cdot\mathbf{n}\,\mathrm{d}\Gamma.$$

2.2. Elastic and acoustic linear wave propagation models

The goal of this subsection is to recall the standard models – and to introduce their associated notations – for elastic and acoustic linear wave propagation. Readers can refer to the following textbooks [18] or [19] for more details or a comprehensive presentation on wave propagation modelling.

Let us denote by $T > 0$ the maximal time of interest and $t \in [0;T]$ the time variable. Within the solid domain, we consider $\mathbf{u}$ the space and time dependent material displacement generated by the high-frequency and low amplitude waves during their course. Internal mechanical stresses $\boldsymbol{\sigma}$ are associated to this displacement. As is standard in ultrasonic wave propagation modeling, we assume a fully linear constitutive law, and in the particular case of this paper we consider – without loss of generality – an isotropic material. In this context we use Hooke's law

$$\boldsymbol{\sigma}(\mathbf{u}) = \lambda \mathrm{tr}(\boldsymbol{\varepsilon}(\mathbf{u}))\mathbf{I} + 2\mu\boldsymbol{\varepsilon}(\mathbf{u}),$$

where $\boldsymbol{\varepsilon}(\mathbf{u}) = \frac{1}{2}\big(\boldsymbol{\nabla}\mathbf{u} + \boldsymbol{\nabla}\mathbf{u}^{\intercal}\big)$ is the linearized Green – Lagrange tensor associated to the displacement $\mathbf{u}$, $\mathrm{tr}(\cdot)$ is the trace of a second order tensor, $\mathbf{I}$ is the identity second order tensor, and $\{\lambda, \mu\}$ are the Lamé's coefficients. In addition to this constitutive law, we recall the standard linear elasto-dynamic equation

$$\rho_{\mathrm{s}}\partial_{tt}^2\mathbf{u} - \boldsymbol{\nabla}\cdot\boldsymbol{\sigma}(\mathbf{u}) = 0, \quad \text{in} \quad \Omega_{\mathrm{s}}, \tag{2}$$

where $\boldsymbol{\nabla}\cdot$ is the divergence operator applied to second order tensors, and ρ_{s} is the mass density of the material.

Within the fluid domain, we consider $\mathbf{v}$ the velocity field and p the pressure field associated to the acoustic wave propagation. They are linked through the standard equations

$$\frac{1}{\rho_{\mathrm{f}}c^2}\partial_t p + \nabla\cdot\mathbf{v} = 0, \quad \rho_{\mathrm{f}}\partial_t\mathbf{v} + \nabla p = 0, \quad \text{in} \quad \Omega_{\mathrm{f}}, \tag{3}$$

where $\nabla\cdot$ is the divergence operator applied to vector fields, c is the speed of waves in the fluid domain, and ρ_{f} is the mass density of the fluid. Defining ϕ the acoustic velocity potential such that

$$\mathbf{v} = \frac{1}{\rho_{\mathrm{f}}}\boldsymbol{\nabla}\phi, \quad p = -\partial_t\phi, \tag{4}$$

where the second relation is obtained using (3), we recover the traditional second order wave equation

$$\frac{1}{\rho_{\mathrm{f}}c^2}\partial_{tt}^2\phi - \frac{1}{\rho_{\mathrm{f}}}\Delta\phi = 0, \quad \text{in} \quad \Omega_{\mathrm{f}}. \tag{5}$$

In the following, we assume that the generation of acoustic waves in the fluid (typically by an emitting actuator) can be represented by an initial condition in (5), while initial conditions in (2) are supposed to be zero. More precisely, we consider a known function $\phi_0 \in H^1(\Omega_{\mathrm{f}})$ such that

$$\phi|_{t=0} = \phi_0, \quad \partial_t\phi|_{t=0} = 0, \quad \text{and} \quad \mathbf{u}|_{t=0} = \partial_t\mathbf{u}|_{t=0} = 0. \tag{6}$$

2.3. Effective transmission conditions for representing the coating material

To represent the propagation within the coating material, we resort to effective transmission conditions (ETC) as in [9] that we adapt to fluid – solid coupling. To simplify the presentation, we will use extensively the following notation

$$\forall d \in \{1, N\}, \quad \forall \mathbf{f} \in [L^2(\Gamma_{\pm})]^d, \quad \mathbf{f}_{\pm} = \mathbf{f}\circ\boldsymbol{\phi}_{\pm}^{\eta} \in [L^2(\Gamma)]^d.$$

In particular this enables us to define the mechanical fluxes on the middle plane (or line) and associated to the fluid and solid fluxes as follows

$$\boldsymbol{\tau}_+ = -p_+\,\mathbf{n}, \quad \boldsymbol{\tau}_- = \boldsymbol{\sigma}_-\cdot\mathbf{n}, \quad \text{on} \quad \Gamma.$$

The mean value and jump of the fluxes are denoted by

$$\langle\boldsymbol{\tau}\rangle = \frac{\boldsymbol{\tau}_+ + \boldsymbol{\tau}_-}{2}, \quad [\boldsymbol{\tau}] = \boldsymbol{\tau}_+ - \boldsymbol{\tau}_-. \tag{7}$$

In the same manner, we define the mean value and jump of velocities on Γ as

$$\langle \mathbf{v} \rangle = \frac{\mathbf{v}_+ + \partial_t \mathbf{u}_-}{2}, \quad [\mathbf{v}] = \mathbf{v}_+ - \partial_t \mathbf{u}_-. \tag{8}$$

Without the presence of the coating layer, implying in particular that $\boldsymbol{\phi}^\eta_\pm$ are identity mappings, satisfying the standard fluid – solid transmission conditions implies

$$[\mathbf{v}] \cdot \mathbf{n} = 0, \quad [\boldsymbol{\tau}] = 0, \quad \text{on} \quad \Gamma,$$

which are the continuity of the normal velocities and the mechanical fluxes. Note that, because of the form of the fluid flux, this is equivalent to satisfying

$$[\mathbf{v}] \cdot \mathbf{n} = 0, \quad [\boldsymbol{\tau}] \cdot \mathbf{n} = 0, \quad \boldsymbol{\tau}_- \cdot \mathbf{n}^\perp = 0, \quad \text{on} \quad \Gamma,$$

where $\mathbf{n}^\perp$ is any tangent vector of Γ. The underlying idea behind ETC, as in [9, 10], is to perturb the two jump relations with spring – mass terms using the mean fluxes and velocities, namely

$$[\mathbf{v}] \cdot \mathbf{n} = \eta \mathrm{s}\, \partial_t \langle \boldsymbol{\tau} \rangle \cdot \mathbf{n}, \quad [\boldsymbol{\tau}] \cdot \mathbf{n} = \eta \mathrm{m}\, \partial_t \langle \mathbf{v} \rangle \cdot \mathbf{n}, \quad \text{on} \quad \Gamma. \tag{9}$$

Here s and m are the effective normal compliance and mass density of the coating layer. As an illustrative example, in the case of an isotropic coating material in 2D admitting $\{\lambda', \mu'\}$ as Lamé's parameters and ρ' as mass density, a typical choice of effective parameters is

$$\mathrm{s} = \frac{1}{\lambda' + 2\mu'}, \quad \mathrm{m} = \rho'. \tag{10}$$

In the following, to simplify the presentation, we will assume that both the thickness η and the effective parameters $\{\mathrm{s}, \mathrm{m}\}$ are constant *w.r.t.* space variables.

Remark 1. *For any vector field* $\mathbf{f}$ *defined on* Ω^η*, the term* $1/\eta\, [\mathbf{f}] \cdot \mathbf{n}$ *can be interpreted as a centered approximation of* $\partial_\mathrm{n} \mathbf{f}$*, the normal derivative at the mid-line or mid-plane. Hence, equations in* (9) *are the centered approximation of*

$$\partial_t \boldsymbol{\tau} \cdot \mathbf{n} = \mathrm{c}\, \partial_\mathrm{n} \mathbf{v}, \quad \mathrm{m}\, \partial_t \mathbf{v} \cdot \mathbf{n} - \partial_\mathrm{n} \boldsymbol{\tau} = 0, \quad \textit{on} \quad \Gamma,$$

where $\mathrm{c} = \mathrm{s}^{-1}$ *is the effective elastic modulus. These relations are nothing more than the expression of the constitutive law and the propagator within the coating layer in the normal direction.*

Remark 2. *Beside verifying the soundness of the effective relations* (9)*, the previous remark can be used to extend these relations to visco-elasticity. Typically, assuming that* d *is a given effective viscous parameter associated to the coating material, we can derive the well-known Kelvin-Voigt, Maxwell and Zener transmission conditions respectively as*

$$\begin{vmatrix} \eta \partial_t \langle \boldsymbol{\tau} \rangle \cdot \mathbf{n} & = \mathrm{c}\, [\mathbf{v}] \cdot \mathbf{n} + \mathrm{d}\, \partial_t [\mathbf{v}] \cdot \mathbf{n}, & \textit{(Kelvin-Voigt)} \\ \eta \left(\mathrm{s}\, \partial_t \langle \boldsymbol{\tau} \rangle \cdot \mathbf{n} + \mathrm{h}\, \langle \boldsymbol{\tau} \rangle \cdot \mathbf{n} \right) & = [\mathbf{v}] \cdot \mathbf{n}, & \textit{(Maxwell)} \\ \eta \left(\partial_t \langle \boldsymbol{\tau} \rangle \cdot \mathbf{n} \ + \tau^{\mathrm{zn}} \partial^2_{tt} \langle \boldsymbol{\tau} \rangle \cdot \mathbf{n} \right) & = \mathrm{c}\, [\mathbf{v}] \cdot \mathbf{n} + \tau^{\mathrm{zn}} \mathrm{d}\, \partial_t [\mathbf{v}] \cdot \mathbf{n}, & \textit{(Zener)} \end{vmatrix}$$

where $\mathrm{h} = \mathrm{d}^{-1}$*, and* τ^{zn} *is a relaxation time associated to the Zener model – see [11, 20, 21] and references therein for more details on visco-elastic wave propagation models.*

2.4. Mortar elements and coupled weak formulation

The mortar element method [1, 2, 3, 4, 5] is originally a domain decomposition approach enabling coupling of non-conforming space discretizations. Recently [11] it has been used to incorporate ETC between two solids and we extend this approach to fluid – solid coupling. To start with, we define the following unknowns

$$\partial_t \lambda_\mathrm{f} = \mathbf{v}_+ \cdot \mathbf{n}, \quad \partial_t \lambda_\mathrm{s} = \boldsymbol{\tau}_- \cdot \mathbf{n}, \tag{11}$$

which are, for any fixed time value, elements of $L^2(\Gamma)$.

Lemma 2. *Assuming that $\Gamma_\pm$ are translations of Γ and imposing free surface boundary conditions on the boundaries $\partial\Omega_\mathrm{f}\backslash\Gamma_+$ and $\partial\Omega_\mathrm{s}\backslash\Gamma_-$, the weak formulation incorporating ETCs with mortar unknowns reads, for any time $t\in]0;T]$,*

Find $\{\phi(t),\mathbf{u}(t),\lambda_\mathrm{f}(t),\lambda_\mathrm{s}(t)\}\in H^1(\Omega_\mathrm{f})\times[H^1(\Omega_\mathrm{s})]^N\times L^2(\Gamma)\times L^2(\Gamma)$ such that

$$\left|\begin{array}{l}
\dfrac{\mathrm{d}^2}{\mathrm{d}t^2}\displaystyle\int_{\Omega_\mathrm{f}}\tfrac{1}{\rho_\mathrm{f}c^2}\,\phi\,\phi^\star\,\mathrm{d}\Omega+\int_{\Omega_\mathrm{f}}\tfrac{1}{\rho_\mathrm{f}}\boldsymbol{\nabla}\phi\cdot\boldsymbol{\nabla}\phi^\star\,\mathrm{d}\Omega+\dfrac{\mathrm{d}}{\mathrm{d}t}\displaystyle\int_\Gamma\lambda_\mathrm{f}\,\phi_+^\star\,\mathrm{d}\Gamma=\int_{\Omega_\mathrm{f}}f\,\phi^\star\,\mathrm{d}\Omega,\\
\dfrac{\mathrm{d}^2}{\mathrm{d}t^2}\displaystyle\int_{\Omega_\mathrm{s}}\rho_\mathrm{s}\mathbf{u}\cdot\mathbf{u}^\star\,\mathrm{d}\Omega+\int_{\Omega_\mathrm{s}}\boldsymbol{\sigma}(\mathbf{u}):\boldsymbol{\varepsilon}(\mathbf{u}^\star)\,\mathrm{d}\Omega-\dfrac{\mathrm{d}}{\mathrm{d}t}\displaystyle\int_\Gamma\lambda_\mathrm{s}\,\mathbf{u}_-^\star\cdot\mathbf{n}\,\mathrm{d}\Gamma=0,\\
\dfrac{\mathrm{d}}{\mathrm{d}t}\displaystyle\int_\Gamma\eta\mathrm{m}\Big(\frac{\lambda_\mathrm{f}+\mathbf{u}_-\cdot\mathbf{n}}{2}\Big)\lambda_\mathrm{f}^\star\,\mathrm{d}\Gamma=\int_\Gamma(\phi_+-\lambda_\mathrm{s})\lambda_\mathrm{f}^\star\,\mathrm{d}\Gamma,\\
\dfrac{\mathrm{d}}{\mathrm{d}t}\displaystyle\int_\Gamma\eta\mathrm{s}\Big(\frac{\phi_++\lambda_\mathrm{s}}{2}\Big)\lambda_\mathrm{s}^\star\,\mathrm{d}\Gamma=\int_\Gamma(\lambda_\mathrm{f}-\mathbf{u}_-\cdot\mathbf{n})\lambda_\mathrm{s}^\star\,\mathrm{d}\Gamma,
\end{array}\right.\tag{12}$$

for any set of test functions $\{\phi^\star,\mathbf{u}^\star,\lambda_\mathrm{f}^\star,\lambda_\mathrm{s}^\star\}\in H^1(\Omega_\mathrm{f})\times[H^1(\Omega_\mathrm{s})]^N\times L^2(\Gamma)\times L^2(\Gamma)$. The initial conditions for the volume unknowns are given by (6)*, and assuming that $\phi_0|_\Gamma=0$, we have*

$$\lambda_\mathrm{f}|_{t=0}=\lambda_\mathrm{s}|_{t=0}=0.$$

Proof. Starting from the strong formulation (5), applying Green's formula and using free surface conditions we get

$$\frac{\mathrm{d}^2}{\mathrm{d}t^2}\int_{\Omega_\mathrm{f}}\tfrac{1}{\rho_\mathrm{f}c^2}\,\phi\,\phi^\star\,\mathrm{d}\Omega+\int_{\Omega_\mathrm{f}}\tfrac{1}{\rho_\mathrm{f}}\boldsymbol{\nabla}\phi\cdot\boldsymbol{\nabla}\phi^\star\,\mathrm{d}\Omega-\int_{\Gamma_+}(\tfrac{1}{\rho_\mathrm{f}}\boldsymbol{\nabla}\phi\cdot\mathbf{n}_+)\,\phi^\star\,\mathrm{d}\Gamma=\int_{\Omega_\mathrm{f}}f\,\phi^\star\,\mathrm{d}\Omega,$$

for any $\phi^\star\in H^1(\Omega_\mathrm{f})$. Using successively the definition of the fluid velocity potential (4), Lemma 1, and the definition (11) of the first mortar unknown, the surface term reads

$$-\int_{\Gamma_+}(\tfrac{1}{\rho_\mathrm{f}}\boldsymbol{\nabla}\phi\cdot\mathbf{n}_+)\,\phi^\star\,\mathrm{d}\Gamma=-\int_{\Gamma_+}(\mathbf{v}\cdot\mathbf{n}_+)\,\phi^\star\,\mathrm{d}\Gamma=\int_\Gamma(\mathbf{v}_+\cdot\mathbf{n})\,\phi_+^\star\,\mathrm{d}\Gamma=\frac{\mathrm{d}}{\mathrm{d}t}\int_\Gamma\lambda_\mathrm{f}\,\phi_+^\star\,\mathrm{d}\Gamma,$$

leading to the first relation in (12). In the same manner, from the strong formulation (2), applying Green's formula and using free surface conditions leads to

$$\frac{\mathrm{d}^2}{\mathrm{d}t^2}\int_{\Omega_\mathrm{s}}\rho_\mathrm{s}\mathbf{u}\cdot\mathbf{u}^\star\,\mathrm{d}\Omega+\int_{\Omega_\mathrm{s}}\boldsymbol{\sigma}(\mathbf{u}):\boldsymbol{\varepsilon}(\mathbf{u}^\star)\,\mathrm{d}\Omega-\int_{\Gamma_-}(\boldsymbol{\sigma}\cdot\mathbf{n}_-)\cdot\mathbf{u}^*\,\mathrm{d}\Gamma=0,$$

for any $\mathbf{u}^*\in[H^1(\Omega_\mathrm{s})]^N$. Using Lemma 1 the surface term becomes

$$\int_{\Gamma_-}(\boldsymbol{\sigma}\cdot\mathbf{n}_-)\cdot\mathbf{u}^*\,\mathrm{d}\Gamma=\int_\Gamma(\boldsymbol{\sigma}_-\cdot\mathbf{n})\cdot\mathbf{u}_-^*\,\mathrm{d}\Gamma=\int_\Gamma\boldsymbol{\tau}_-\cdot\mathbf{u}_-^*\,\mathrm{d}\Gamma.$$

Using the fact that $\boldsymbol{\tau}_-\cdot\mathbf{n}^\perp=0$, and the definition (11) of the second mortar unknown, we obtain

$$\int_\Gamma\boldsymbol{\tau}_-\cdot\mathbf{u}_-^*\,\mathrm{d}\Gamma=\frac{\mathrm{d}}{\mathrm{d}t}\int_\Gamma\lambda_\mathrm{s}\,\mathbf{u}_-^\star\cdot\mathbf{n}\,\mathrm{d}\Gamma,$$

entailing the second relation in (12). Finally, using the jump relations in (9) and the definition (11) of the mortar unknowns we have

$$\partial_t\lambda_\mathrm{f}-\partial_t\mathbf{u}_-\cdot\mathbf{n}=\eta\mathrm{s}\frac{\partial_{tt}^2\phi_++\partial_{tt}^2\lambda_\mathrm{s}}{2},\quad\partial_t\phi_+-\partial_t\lambda_\mathrm{s}=\eta\mathrm{m}\frac{\partial_{tt}^2\lambda_\mathrm{f}+\partial_{tt}^2\mathbf{u}_-\cdot\mathbf{n}}{2},$$

which leads, after integration in time and in space over Γ to the last two relations in (12). □

2.5. Continuous energy conservation

In order to establish the energy conservation property associated to system (12), we give the following useful relation

$$\big([\boldsymbol{\tau}]\cdot\mathbf{n}\big)\big(\langle\mathbf{v}\rangle\cdot\mathbf{n}\big)+\big(\langle\boldsymbol{\tau}\rangle\cdot\mathbf{n}\big)\big([\mathbf{v}]\cdot\mathbf{n}\big)=\big(\boldsymbol{\tau}_+\cdot\mathbf{n}\big)\big(\mathbf{v}_+\cdot\mathbf{n}\big)-\big(\boldsymbol{\tau}_-\cdot\mathbf{n}\big)\big(\mathbf{v}_-\cdot\mathbf{n}\big), \tag{13}$$

which can be verified using the definition of the means and the jumps in (7) and (8).

Lemma 3. *For any time $t\in[0;T]$, we define the kinetic and potential energy functionals associated to the volume propagators*

$$\mathcal{K}_{\rm f}(t)=\frac{1}{2}\int_{\Omega_f}\frac{1}{\rho_{\rm f}c^2}\partial_t\phi^2\,\mathrm{d}\Omega,\quad \mathcal{P}_{\rm f}(t)=\frac{1}{2}\int_{\Omega_f}\frac{1}{\rho_{\rm f}}|\boldsymbol{\nabla}\phi|^2\,\mathrm{d}\Omega,$$
$$\mathcal{K}_{\rm s}(t)=\frac{1}{2}\int_{\Omega_{\rm s}}\rho_{\rm s}|\partial_t\mathbf{u}|^2\,\mathrm{d}\Omega\ ,\quad \mathcal{P}_{\rm s}(t)=\frac{1}{2}\int_{\Omega_{\rm s}}\boldsymbol{\sigma}(\mathbf{u}):\varepsilon(\mathbf{u})\,\mathrm{d}\Omega,$$

and the kinetic and potential energy functionals associated to the thin layer

$$\mathcal{K}_\eta(t)=\frac{\eta\mathrm{m}}{2}\int_\Gamma\Big(\frac{\partial_t\lambda_{\rm f}+\partial_t\mathbf{u}_-\cdot\mathbf{n}}{2}\Big)^2\mathrm{d}\Gamma,\quad \mathcal{P}_\eta(t)=\frac{\eta\,\mathrm{s}}{2}\int_\Gamma\Big(\frac{\partial_t\phi_++\partial_t\lambda_{\rm s}}{2}\Big)^2\mathrm{d}\Gamma.$$

The total energy functional

$$\mathcal{E}(t)=\mathcal{K}_{\rm f}(t)+\mathcal{P}_{\rm f}(t)+\mathcal{K}_{\rm s}(t)+\mathcal{P}_{\rm s}(t)+\mathcal{K}_\eta(t)+\mathcal{P}_\eta(t),$$

is conserved over time, namely

$$\frac{\mathrm{d}}{\mathrm{d}t}\mathcal{E}(t)=0.$$

Proof. Using $\phi^\star=\partial_t\phi$ and $\mathbf{u}^*=\partial_t\mathbf{u}$ as test functions in the first two relations in (12) and summing directly leads to

$$\frac{\mathrm{d}}{\mathrm{d}t}\Big(\mathcal{K}_{\rm f}+\mathcal{P}_{\rm f}+\mathcal{K}_{\rm s}+\mathcal{P}_{\rm s}\Big)+\int_\Gamma\partial_t\lambda_{\rm f}\,\partial_t\phi_+-\partial_t\lambda_{\rm s}\,\partial_t\mathbf{u}_-\cdot\mathbf{n}\,\mathrm{d}\Gamma=0.$$

We conclude the demonstration by using the definition of the Lagrange unknowns, relation (13) and the effective transmissions (9), namely

$$\begin{aligned}\int_\Gamma\partial_t\lambda_{\rm f}\,\partial_t\phi_+-\partial_t\lambda_{\rm s}\,\partial_t\mathbf{u}_-\cdot\mathbf{n}\,\mathrm{d}\Gamma&=\int_\Gamma\big(\boldsymbol{\tau}_+\cdot\mathbf{n}\big)\big(\mathbf{v}_+\cdot\mathbf{n}\big)-\big(\boldsymbol{\tau}_-\cdot\mathbf{n}\big)\big(\mathbf{v}_-\cdot\mathbf{n}\big)\,\mathrm{d}\Gamma\\&=\int_\Gamma\big([\boldsymbol{\tau}]\cdot\mathbf{n}\big)\big(\langle\mathbf{v}\rangle\cdot\mathbf{n}\big)+\big(\langle\boldsymbol{\tau}\rangle\cdot\mathbf{n}\big)\big([\mathbf{v}]\cdot\mathbf{n}\big)\,\mathrm{d}\Gamma\\&=\int_\Gamma\eta\mathrm{m}\big(\partial_t\langle\mathbf{v}\rangle\cdot\mathbf{n}\big)\big(\langle\mathbf{v}\rangle\cdot\mathbf{n}\big)+\eta\mathrm{s}\big(\partial_t\langle\boldsymbol{\tau}\rangle\cdot\mathbf{n}\big)\big(\langle\boldsymbol{\tau}\rangle\cdot\mathbf{n}\big)\,\mathrm{d}\Gamma\\&=\frac{\mathrm{d}}{\mathrm{d}t}\Big(\mathcal{K}_\eta+\mathcal{P}_\eta\Big).\end{aligned}$$

□

Remark 3. *The energy conservation property is interesting for at least two reasons. First, since the original system (incorporating the exact propagator in the coating layer) is a conservative system (as any inviscid wave propagation system), it seems natural to demand from system* (12) *to respect this property. Second, as we will see in Section 3, this conservation property can also be derived after time and space discretization and it is a fundamental argument to insure stability of the fully discrete scheme – see e.g. [17] and references therein for more detailed discussions.*

3. Stable fully discrete scheme

3.1. Space discretization using spectral finite elements

We discretize in space the weak formulation (12) using spectral finite elements [13]. In its original form, it is a H^1 – conform, high order finite element method, based on quadrangular or hexahedral meshes, with the Gauss – Lobatto distribution of nodes in the reference element. Let us denote by $\mathcal{T}_h(\overline{\Omega}_\mathrm{f})$ and $\mathcal{T}_H(\overline{\Omega}_\mathrm{s})$ conform meshes of the fluid and solid domains with characteristic mesh sizes h and H. In most cases, the gap between wave speeds in the two domains require two different mesh sizes to obtain better performances. Therefore, in the following we assume that $h \leq H$, potentially entailing non-conformities at the coupling interface – see Figure 1 for an illustration of the case $H = 2h$. For each element K in a mesh, we denote by $\mathbf{F}_K$ the associated transformation of the reference quadrangle or hexahedron $\widehat{K}$. On the reference element, we consider $\mathcal{Q}^\alpha(\widehat{K})$ the space of polynomials of maximal order $\alpha \in \mathbb{N}$. Let p and q be two given natural integers, we define the following finite element approximation spaces

$$\left|\begin{array}{ll} V_h &= \Big\{ v_h \in \mathcal{C}^0(\overline{\Omega}_\mathrm{f}) \;\Big|\; \forall K \in \mathcal{T}_h(\overline{\Omega}_\mathrm{f}),\ \exists!\, \widehat{v} \in \mathcal{Q}^p(\widehat{K}),\ v_h|_K = \widehat{v} \circ \mathbf{F}_K^{-1} \Big\} \subset H^1(\Omega_\mathrm{f}), \\ W_H &= \Big\{ w_H \in \mathcal{C}^0(\overline{\Omega}_\mathrm{s}) \;\Big|\; \forall K \in \mathcal{T}_H(\overline{\Omega}_\mathrm{s}),\ \exists!\, \widehat{w} \in \mathcal{Q}^q(\widehat{K}),\ w_H|_K = \widehat{w} \circ \mathbf{F}_K^{-1} \Big\} \subset H^1(\Omega_\mathrm{s}), \end{array}\right.$$

and the vectorial counterpart $\mathbf{W}_H = [W_H]^N \subset [H^1(\Omega_\mathrm{s})]^N$. Let N_f and N_s be the dimension of the approximation spaces V_h and $\mathbf{W}_H$ respectively, we consider

$$V_h = \mathrm{span}\,\{\varphi_I\}_{I=1}^{N_\mathrm{f}}, \quad W_H = \mathrm{span}\,\{\psi_I\}_{I=1}^{N_\mathrm{s}/N}, \quad \mathbf{W}_H = \mathrm{span}\,\{\boldsymbol{\psi}_I\}_{I=1}^{N_\mathrm{s}},$$

the associated Lagrange basis functions. Using these notations, we introduce the mass and stiffness matrices

$$\left|\begin{array}{ll} \mathbb{M}_\mathrm{f} = \Big(\displaystyle\int_{\Omega_\mathrm{f}} \tfrac{1}{\rho_\mathrm{f} c^2}\, \varphi_I\, \varphi_J \,\mathrm{d}\Omega \Big)_{I,J=1}^{N_\mathrm{f}} & , \quad \mathbb{M}_\mathrm{s} = \Big(\displaystyle\int_{\Omega_\mathrm{s}} \rho_\mathrm{s}\, \boldsymbol{\psi}_I \cdot \boldsymbol{\psi}_J \,\mathrm{d}\Omega \Big)_{I,J=1}^{N_\mathrm{s}}, \\ \mathbb{K}_\mathrm{f} = \Big(\displaystyle\int_{\Omega_\mathrm{f}} \tfrac{1}{\rho_\mathrm{f}}\, \boldsymbol{\nabla}\varphi_I \cdot \boldsymbol{\nabla}\varphi_J \,\mathrm{d}\Omega \Big)_{I,J=1}^{N_\mathrm{f}}, & \quad \mathbb{K}_\mathrm{s} = \Big(\displaystyle\int_{\Omega_\mathrm{s}} \boldsymbol{\sigma}(\boldsymbol{\psi}_I) : \boldsymbol{\varepsilon}(\boldsymbol{\psi}_J) \,\mathrm{d}\Omega \Big)_{I,J=1}^{N_\mathrm{s}}. \end{array}\right.$$

For the mortar unknowns, we consider the approximation space built from the trace of the volume space W_H. More precisely, we define

$$X_H = \mathrm{span}\,\{\xi_\ell\}_{\ell=1}^{N_\Gamma} \subset L^2(\Gamma), \quad \forall \ell = 1, \cdots, N_\Gamma, \quad \exists!\, I \in \{1, \cdots, {}^{N_\mathrm{s}}/_N\}, \quad \xi_\ell = \psi_I|_{\Gamma_-} \circ \phi_-^\eta, \tag{14}$$

and N_Γ the number of nodes on Γ_-. We define the coupling matrices (from mortar to volume unknowns) and the surface mass matrix

$$\mathbb{C}_\mathrm{f} = \Big(\int_\Gamma (\varphi_{I+})\, \xi_\ell \,\mathrm{d}\Gamma \Big)_{I,\ell=1}^{N_\mathrm{f},N_\Gamma}, \quad \mathbb{C}_\mathrm{s} = \Big(\int_\Gamma (\boldsymbol{\psi}_{I-}) \cdot \mathbf{n}\, \xi_\ell \,\mathrm{d}\Gamma \Big)_{I,\ell=1}^{N_\mathrm{s},N_\Gamma}, \quad \mathbb{M}_\Gamma = \Big(\int_\Gamma \xi_\ell\, \xi_m \mathrm{d}\Gamma \Big)_{\ell,m=1}^{N_\Gamma}.$$

In practice, for computing the entries of the volume mass matrix $\mathbb{M}_\mathrm{f}$ and $\mathbb{M}_\mathrm{s}$, we use a quadrature formula whose points match the nodes of the local Lagrange polynomials defining the basis functions of V_h and W_H. This is called the "mass lumping" technique [13, 22, 23] since it leads to diagonal mass matrices. It has been the subject of particular interest in the context of finite element methods applied to time domain wave propagation problems, because it enables fully explicit time discretization schemes. In order to conserve stability and accuracy, specific conditions must be enforced on the quadrature points and weights. For quadrangles and hexahedra, these conditions are met at any order of approximations thanks to the Gauss – Lobatto rules [23, 24]. See Figure 1 for a representation of the location of the Gauss – Lobatto points for the case $p = q = 5$. For triangles and tetrahedra dedicated construction of the quadrature formula is needed [25, 26]. In the next lemma, we show that this procedure can be also applied to render diagonal surface mass matrices.

Lemma 4. *Assuming that mass lumping is applied, the matrices* $\mathbb{M}_\Gamma$ *and* $\mathbb{C}_\mathrm{s}^\intercal \mathbb{M}_\mathrm{s}^{-1}\mathbb{C}_\mathrm{s}$ *are diagonal. In the particular case of a conform interface – i.e. a "one-to-one" mapping between the nodes of* $\mathcal{T}_h(\overline{\Omega}_\mathrm{f})$ *and* $\mathcal{T}_H(\overline{\Omega}_\mathrm{s})$ *at the interface – the matrix* $\mathbb{C}_\mathrm{f}^\intercal \mathbb{M}_\mathrm{f}^{-1}\mathbb{C}_\mathrm{f}$ *is also diagonal.*

Proof. A precise demonstration would require a substantial amount of notations for the volume and surface discrete spaces. Instead we give hereafter the main arguments for the two dimensional case, and refer to [15] for more details for the fluid – fluid case.

Using the same arguments as for volume mass lumping – see [13, 22, 23] – one can easily verify that matching the quadrature points on each surface elements with the nodes defining the local Lagrange polynomials leads to a diagonal surface mass matrix $\mathbb{M}_\Gamma$. Further more, as defined in (14), the approximation space for the mortar unknown is the trace space of the solid volume approximation space. Hence, applying mass lumping for the integration of the entries of $\mathbb{C}_\mathrm{s}$ leads – up to a recombination of the DoFs indexes to separate the boundary from the interior – to a matrix with the following form

$$\mathbb{C}_\mathrm{s} = \begin{pmatrix} \mathbb{C}_{\mathrm{s},1} \\ \mathbb{C}_{\mathrm{s},2} \\ 0 \end{pmatrix}. \tag{15}$$

The two upper blocks $\mathbb{C}_{\mathrm{s},1}$ and $\mathbb{C}_{\mathrm{s},2}$ are of size $N_\Gamma \times N_\Gamma$ and are mass matrices weighted with the first and second components of the normal vector field of the interface respectively. As such they can be lumped into diagonal matrices. The lower block represents the interactions of the surface basis functions with the interior basis functions which are necessarily zero when mass lumping is applied. From this decomposition and using the fact that the volume mass matrix is also diagonal, we have

$$\mathbb{C}_\mathrm{s}^\intercal \mathbb{M}_\mathrm{s}^{-1}\mathbb{C}_\mathrm{s} = \mathbb{C}_{\mathrm{s},1}^\intercal \mathbb{M}_{\mathrm{s},\Gamma\Gamma}^{-1}\mathbb{C}_{\mathrm{s},1} + \mathbb{C}_{\mathrm{s},2}^\intercal \mathbb{M}_{\mathrm{s},\Gamma\Gamma}^{-1}\mathbb{C}_{\mathrm{s},2},$$

where $\mathbb{M}_{\mathrm{s},\Gamma\Gamma}$ is the block of the diagonal mass matrix associated to the boundary DoFs. In the right hand side of this expression, only diagonal matrices appear, hence $\mathbb{C}_\mathrm{s}^\intercal \mathbb{M}_\mathrm{s}^{-1}\mathbb{C}_\mathrm{s}$ is diagonal. In the particular case of a conform interface, the trace space of the fluid approximation space matches the one of the solid approximation space. Hence we have a similar decomposition (15) for $\mathbb{C}_\mathrm{f}$ when mass lumping is applied, namely

$$\mathbb{C}_\mathrm{f} = \begin{pmatrix} \mathbb{M}_\Gamma \\ 0 \end{pmatrix},$$

where the upper block simply is the surface mass matrix. This entails directly that $\mathbb{C}_\mathrm{f}^\intercal \mathbb{M}_\mathrm{f}^{-1}\mathbb{C}_\mathrm{f}$ is diagonal and concludes the proof. □

3.2. Time discretization

Let us consider $\Delta t > 0$ a given time step – satisfying a specific stability condition discussed in the next subsection – and $n \in \mathbb{N}$ any step index such that $t^n = n\Delta t \in [0; T]$. We consider $\overrightarrow{\phi}^n \in \mathbb{R}^{N_\mathrm{f}}$ the vector of components of the discrete velocity potential in the basis of V_h at time t^n. In the same manner we define $\overrightarrow{u}^n \in \mathbb{R}^{N_\mathrm{s}}$, $\overrightarrow{\lambda}_\mathrm{f}^n \in \mathbb{R}^{N_\Gamma}$ and $\overrightarrow{\lambda}_\mathrm{s}^n \in \mathbb{R}^{N_\Gamma}$ the vectors of degrees of freedom in the basis of the relevant approximation spaces. With these notations, for the time discretization, we apply an explicit second order time-scheme centered at t^n for the volume propagators, and a second order time-scheme centered at $t^{n+1/2}$ for the transmission conditions, namely

$$\left|\begin{array}{l} \frac{1}{\Delta t^2}\mathbb{M}_\mathrm{f}\big(\overrightarrow{\phi}^{n+1} - 2\overrightarrow{\phi}^n + \overrightarrow{\phi}^{n-1}\big) + \mathbb{K}_\mathrm{f}\overrightarrow{\phi}^n + \frac{1}{2\Delta t}\mathbb{C}_\mathrm{f}\big(\overrightarrow{\lambda}_\mathrm{f}^{n+1} - \overrightarrow{\lambda}_\mathrm{f}^{n-1}\big) = 0, \\ \frac{1}{\Delta t^2}\mathbb{M}_\mathrm{s}\big(\overrightarrow{u}^{n+1} - 2\overrightarrow{u}^n + \overrightarrow{u}^{n-1}\big) + \mathbb{K}_\mathrm{s}\overrightarrow{u}^n - \frac{1}{2\Delta t}\mathbb{C}_\mathrm{s}\big(\overrightarrow{\lambda}_\mathrm{s}^{n+1} - \overrightarrow{\lambda}_\mathrm{s}^{n-1}\big) = 0, \\ \frac{\eta_\mathrm{m}}{2\Delta t}\mathbb{M}_\Gamma\big(\overrightarrow{\lambda}_\mathrm{f}^{n+1} - \overrightarrow{\lambda}_\mathrm{f}^{n}\big) + \frac{\eta_\mathrm{m}}{2\Delta t}\mathbb{C}_\mathrm{s}^\intercal\big(\overrightarrow{u}^{n+1} - \overrightarrow{u}^{n}\big) = \frac{1}{2}\mathbb{C}_\mathrm{f}^\intercal\big(\overrightarrow{\phi}^{n+1} + \overrightarrow{\phi}^{n}\big) - \frac{1}{2}\mathbb{M}_\Gamma\big(\overrightarrow{\lambda}_\mathrm{s}^{n+1} + \overrightarrow{\lambda}_\mathrm{s}^{n}\big), \\ \frac{\eta_\mathrm{s}}{2\Delta t}\mathbb{C}_\mathrm{f}^\intercal\big(\overrightarrow{\phi}^{n+1} - \overrightarrow{\phi}^{n}\big) + \frac{\eta_\mathrm{s}}{2\Delta t}\mathbb{M}_\Gamma\big(\overrightarrow{\lambda}_\mathrm{s}^{n+1} - \overrightarrow{\lambda}_\mathrm{s}^{n}\big) = \frac{1}{2}\mathbb{M}_\Gamma\big(\overrightarrow{\lambda}_\mathrm{f}^{n+1} + \overrightarrow{\lambda}_\mathrm{f}^{n}\big) - \frac{1}{2}\mathbb{C}_\mathrm{s}^\intercal\big(\overrightarrow{u}^{n+1} + \overrightarrow{u}^{n}\big). \end{array}\right. \tag{16}$$

System (16) is completed with initial steps deduced from the initial conditions of the time continuous dynamics (12). More precisely, denoting by $\overrightarrow{\phi}_0$ the discrete representation of the initial condition ϕ_0 in the approximation space V_h, we have

$$\overrightarrow{\phi}^0 = \overrightarrow{\phi}_0, \quad \overrightarrow{\phi}^1 = 0, \quad \overrightarrow{u}^0 = \overrightarrow{u}^1 = 0, \quad \text{and} \quad \overrightarrow{\lambda}_{\mathrm{f}}^0 = \overrightarrow{\lambda}_{\mathrm{f}}^1 = \overrightarrow{\lambda}_{\mathrm{s}}^0 = \overrightarrow{\lambda}_{\mathrm{s}}^1 = 0. \tag{17}$$

3.3. Fully discrete energy conservation

The stability analysis proposed here follows standard energy arguments, see [17]. In essence, we start by proving that a functional is conserved by the fully-discrete scheme, and we find the condition on the time step for this functional to be positive. To do so, we will use the following notation: for any (semi)-definite positive matrix $\mathbb{A}$ we denote by $\|\cdot\|_{\mathbb{A}}$ its associated (semi)-norm.

Lemma 5. *For any step index n, we define the kinetic and potential functionals associated to the volume propagators*

$$\mathbf{K}_{\mathrm{f}}^{n+1/2} = \frac{1}{2}\Big\|\frac{\overrightarrow{\phi}^{n+1} - \overrightarrow{\phi}^{n}}{\Delta t}\Big\|_{\mathbb{M}_{\mathrm{f}}}^2, \quad \mathbf{P}_{\mathrm{f}}^{n+1/2} = \frac{1}{2}\overrightarrow{\phi}^{n+1\intercal}\mathbb{K}_{\mathrm{f}}\overrightarrow{\phi}^{n},$$
$$\mathbf{K}_{\mathrm{s}}^{n+1/2} = \frac{1}{2}\Big\|\frac{\overrightarrow{u}^{n+1} - \overrightarrow{u}^{n}}{\Delta t}\Big\|_{\mathbb{M}_{\mathrm{s}}}^2, \quad \mathbf{P}_{\mathrm{s}}^{n+1/2} = \frac{1}{2}\overrightarrow{u}^{n+1\intercal}\mathbb{K}_{\mathrm{s}}\overrightarrow{u}^{n},$$

and the kinetic and potential functionals associated to the thin layer

$$\mathbf{K}_{\eta}^{n+1/2} = \frac{\eta \mathrm{m}}{2}\Big\|\frac{1}{2}\frac{\overrightarrow{\lambda}_{\mathrm{f}}^{n+1} - \overrightarrow{\lambda}_{\mathrm{f}}^{n}}{\Delta t} + \frac{1}{2}\mathbb{M}_{\Gamma}^{-1}\mathbb{C}_{\mathrm{s}}^{\intercal}\frac{\overrightarrow{u}^{n+1} - \overrightarrow{u}^{n}}{\Delta t}\Big\|_{\mathbb{M}_{\Gamma}}^2,$$
$$\mathbf{P}_{\eta}^{n+1/2} = \frac{\eta \mathrm{s}}{2}\Big\|\frac{1}{2}\frac{\overrightarrow{\lambda}_{\mathrm{s}}^{n+1} - \overrightarrow{\lambda}_{\mathrm{s}}^{n}}{\Delta t} + \frac{1}{2}\mathbb{M}_{\Gamma}^{-1}\mathbb{C}_{\mathrm{f}}^{\intercal}\frac{\overrightarrow{\phi}^{n+1} - \overrightarrow{\phi}^{n}}{\Delta t}\Big\|_{\mathbb{M}_{\Gamma}}^2.$$

The total energy functional

$$\mathbf{E}^{n+1/2} = \mathbf{K}_{\mathrm{f}}^{n+1/2} + \mathbf{P}_{\mathrm{f}}^{n+1/2} + \mathbf{K}_{\mathrm{s}}^{n+1/2} + \mathbf{P}_{\mathrm{s}}^{n+1/2} + \mathbf{K}_{\eta}^{n+1/2} + \mathbf{P}_{\eta}^{n+1/2} \tag{18}$$

satisfies the following conservation property

$$\frac{\mathbf{E}^{n+1/2} - \mathbf{E}^{n-1/2}}{\Delta t} = 0.$$

Proof. Multiplying the first and second relation of (16) by the centered discrete time-derivative of the potential and displacement respectively, and summing the two relations leads to

$$\frac{\mathbf{K}_{\mathrm{f}}^{n+1/2} - \mathbf{K}_{\mathrm{f}}^{n-1/2}}{\Delta t} + \frac{\mathbf{P}_{\mathrm{f}}^{n+1/2} - \mathbf{P}_{\mathrm{f}}^{n-1/2}}{\Delta t} + \frac{\mathbf{K}_{\mathrm{s}}^{n+1/2} - \mathbf{K}_{\mathrm{s}}^{n-1/2}}{\Delta t} + \frac{\mathbf{P}_{\mathrm{s}}^{n+1/2} - \mathbf{P}_{\mathrm{s}}^{n-1/2}}{\Delta t} +$$
$$\Big(\frac{\overrightarrow{\phi}^{n+1} - \overrightarrow{\phi}^{n-1}}{2\Delta t}\Big)^{\intercal}\mathbb{C}_{\mathrm{f}}\Big(\frac{\overrightarrow{\lambda}_{\mathrm{f}}^{n+1} - \overrightarrow{\lambda}_{\mathrm{f}}^{n-1}}{2\Delta t}\Big) - \Big(\frac{\overrightarrow{u}^{n+1} - \overrightarrow{u}^{n-1}}{2\Delta t}\Big)^{\intercal}\mathbb{C}_{\mathrm{s}}\Big(\frac{\overrightarrow{\lambda}_{\mathrm{s}}^{n+1} - \overrightarrow{\lambda}_{\mathrm{s}}^{n-1}}{2\Delta t}\Big) = 0.$$

The remaining part of the demonstration aims at reformulating the last term in the previous equation. Computing the time difference of the third relation in (16) at times $t^{n+1/2}$ and $t^{n-1/2}$, and multiplying by the discrete mean velocity entails

$$\frac{1}{2}\Big(\frac{\overrightarrow{\lambda}_{\mathrm{f}}^{n+1} - \overrightarrow{\lambda}_{\mathrm{f}}^{n-1}}{2\Delta t} + \mathbb{M}_{\Gamma}^{-1}\mathbb{C}_{\mathrm{s}}^{\intercal}\frac{\overrightarrow{u}^{n+1} - \overrightarrow{u}^{n-1}}{2\Delta t}\Big)^{\intercal}\mathbb{M}_{\Gamma}\Big(\mathbb{M}_{\Gamma}^{-1}\mathbb{C}_{\mathrm{f}}^{\intercal}\frac{\overrightarrow{\phi}^{n+1} - \overrightarrow{\phi}^{n-1}}{2\Delta t} - \frac{\overrightarrow{\lambda}_{\mathrm{s}}^{n+1} - \overrightarrow{\lambda}_{\mathrm{s}}^{n-1}}{2\Delta t}\Big)$$
$$= \frac{\mathbf{K}_{\eta}^{n+1/2} - \mathbf{K}_{\eta}^{n-1/2}}{\Delta t}.$$

In the same manner, computing the time difference of the fourth relation in (16) at times $t^{n+1/2}$ and $t^{n-1/2}$, and multiplying by the discrete mean flux entails

$$\frac{1}{2}\Big(\mathbb{M}_\Gamma^{-1}\mathbb{C}_\mathrm{f}^\intercal\frac{\overrightarrow{\phi}^{n+1}-\overrightarrow{\phi}^{n-1}}{2\Delta t}+\frac{\overrightarrow{\lambda}_\mathrm{s}^{n+1}-\overrightarrow{\lambda}_\mathrm{s}^{n-1}}{2\Delta t}\Big)^\intercal\mathbb{M}_\Gamma\Big(\frac{\overrightarrow{\lambda}_\mathrm{f}^{n+1}-\overrightarrow{\lambda}_\mathrm{f}^{n-1}}{2\Delta t}-\mathbb{M}_\Gamma^{-1}\mathbb{C}_\mathrm{s}^\intercal\frac{\overrightarrow{u}^{n+1}-\overrightarrow{u}^{n-1}}{2\Delta t}\Big)$$
$$=\frac{\mathbf{P}_\eta^{n+1/2}-\mathbf{P}_\eta^{n-1/2}}{\Delta t}.$$

Finally, by summing the left hand sides of the two previous equations and after straightforward simplifications – that are the exact fully discrete translation of the relation (13) – we obtain

$$\Big(\frac{\overrightarrow{\phi}^{n+1}-\overrightarrow{\phi}^{n-1}}{2\Delta t}\Big)^\intercal\mathbb{C}_\mathrm{f}\Big(\frac{\overrightarrow{\lambda}_\mathrm{f}^{n+1}-\overrightarrow{\lambda}_\mathrm{f}^{n-1}}{2\Delta t}\Big)-\Big(\frac{\overrightarrow{u}^{n+1}-\overrightarrow{u}^{n-1}}{2\Delta t}\Big)^\intercal\mathbb{C}_\mathrm{s}\Big(\frac{\overrightarrow{\lambda}_\mathrm{s}^{n+1}-\overrightarrow{\lambda}_\mathrm{s}^{n-1}}{2\Delta t}\Big)=$$
$$\frac{\mathbf{K}_\eta^{n+1/2}-\mathbf{K}_\eta^{n-1/2}}{\Delta t}+\frac{\mathbf{P}_\eta^{n+1/2}-\mathbf{P}_\eta^{n-1/2}}{\Delta t},$$

completing the proof of the sought conservation property. □

3.4. Stability analysis of the fully discrete scheme

In this section we derive a sufficient condition on the time step that insures stability of the fully discrete scheme (16). To do so, we adapt energy arguments followed for instance in [17] or [27], which boils down to two steps. First we find the condition for the discrete total energy (18) to be a positive functional, which is the goal of the following lemma. Second we derive a stability result from the positivity of the energy functional.

Lemma 6. *Defining*

$$\overline{\Delta t}=\min\left\{\frac{2}{\sqrt{r(\mathbb{M}_\mathrm{f}^{-1}\mathbb{K}_\mathrm{f})}},\frac{2}{\sqrt{r(\mathbb{M}_\mathrm{s}^{-1}\mathbb{K}_\mathrm{s})}}\right\},\tag{19}$$

where $r(\cdot)$ is the spectral radius of a matrix, the discrete total energy (18) *is a sum of positive functionals upon the following condition*

$$\Delta t\leq\overline{\Delta t}.$$

Proof. The kinetic and potential functionals associated to the thin layer are necessarily positive terms, hence they do not require specific treatment – this is mainly a consequence to the fact that an implicit time scheme has been used for time-discretization of the ETCs. Focusing on the volume discrete propagator and starting with the fluid domain functionals, one can reformulate

$$\mathbf{K}_\mathrm{f}^{n+1/2}+\mathbf{P}_\mathrm{f}^{n+1/2}=\frac{1}{2}\Big\|\frac{\overrightarrow{\phi}^{n+1}-\overrightarrow{\phi}^{n}}{\Delta t}\Big\|_{\widetilde{\mathbb{M}}_\mathrm{f}}^2+\frac{1}{2}\Big\|\frac{\overrightarrow{\phi}^{n+1}+\overrightarrow{\phi}^{n}}{2}\Big\|_{\mathbb{K}_\mathrm{f}}^2,\quad\text{with}\quad\widetilde{\mathbb{M}}_\mathrm{f}=\mathbb{M}_\mathrm{f}-\frac{\Delta t^2}{4}\mathbb{K}_\mathrm{f}.\tag{20}$$

Therefore, we can insure that it is a positive matrix upon the following condition

$$\Delta t\leq\frac{2}{\sqrt{r(\mathbb{M}_\mathrm{f}^{-1}\mathbb{K}_\mathrm{f})}}.$$

Operating in the same fashion for the solid domain concludes the proof. □

Theorem 1. *Assuming that $\Delta t<\overline{\Delta t}$, then there exists a constant $C_0>0$ that depends on the global time window, the time step, the effective parameters and the initial steps such that*

$$\forall n\geq 1,\quad\Big(\|\overrightarrow{\phi}^{n+1}\|_{\mathbb{M}_\mathrm{f}}^2+\|\overrightarrow{u}^{n+1}\|_{\mathbb{M}_\mathrm{s}}^2+\|\overrightarrow{\lambda}_\mathrm{f}^{n+1}\|_{\mathbb{M}_\Gamma}^2+\|\overrightarrow{\lambda}_\mathrm{s}^{n+1}\|_{\mathbb{M}_\Gamma}^2\Big)^{1/2}\leq C_0.\tag{21}$$

Proof. Let us start with the mortar unknowns. Using the simple relation $a^2 + b^2 \leq (a+b)^2$ for any real values a and b with positive product, we obtain

$$\begin{aligned}\frac{\eta\mathrm{m}}{8}\Big\|\frac{\overrightarrow{\lambda}_{\mathrm{f}}^{n+1}-\overrightarrow{\lambda}_{\mathrm{f}}^{n}}{\Delta t}\Big\|_{\mathbb{M}_\Gamma}^2 &\leq \frac{\eta\mathrm{m}}{2}\Big\|\frac{1}{2}\frac{\overrightarrow{\lambda}_{\mathrm{f}}^{n+1}-\overrightarrow{\lambda}_{\mathrm{f}}^{n}}{\Delta t}\Big\|_{\mathbb{M}_\Gamma}^2 + \frac{\eta\mathrm{m}}{2}\Big\|\frac{1}{2}\mathbb{M}_\Gamma^{-1}\mathbb{C}_{\mathrm{s}}^{\intercal}\frac{\overrightarrow{u}^{n+1}-\overrightarrow{u}^{n}}{\Delta t}\Big\|_{\mathbb{M}_\Gamma}^2\\ &\leq \frac{\eta\mathrm{m}}{2}\Big\|\frac{1}{2}\frac{\overrightarrow{\lambda}_{\mathrm{f}}^{n+1}-\overrightarrow{\lambda}_{\mathrm{f}}^{n}}{\Delta t} + \frac{1}{2}\mathbb{M}_\Gamma^{-1}\mathbb{C}_{\mathrm{s}}^{\intercal}\frac{\overrightarrow{u}^{n+1}-\overrightarrow{u}^{n}}{\Delta t}\Big\|_{\mathbb{M}_\Gamma}^2 = \mathbf{K}_\eta^{n+1/2}.\end{aligned}$$

Upon the assumption that $\Delta t < \overline{\Delta t}$, we can invoke Lemma 6 to insure that the total discrete energy is a sum of positive functionals, leading to

$$\Big\|\frac{\overrightarrow{\lambda}_{\mathrm{f}}^{n+1}-\overrightarrow{\lambda}_{\mathrm{f}}^{n}}{\Delta t}\Big\|_{\mathbb{M}_\Gamma}^2 \leq \frac{8}{\eta\mathrm{m}}\mathbf{E}^{n+1/2}.$$

Using this estimation and the energy conservation property provided by Lemma 5 entails

$$\begin{aligned}\|\overrightarrow{\lambda}_{\mathrm{f}}^{n+1}\|_{\mathbb{M}_\Gamma} \leq \Delta t\Big\|\frac{\overrightarrow{\lambda}_{\mathrm{f}}^{n+1}-\overrightarrow{\lambda}_{\mathrm{f}}^{n}}{\Delta t}\Big\|_{\mathbb{M}_\Gamma} + \|\overrightarrow{\lambda}_{\mathrm{f}}^{n}\|_{\mathbb{M}_\Gamma} &\leq \Delta t\sqrt{\frac{8}{\eta\mathrm{m}}\mathbf{E}^{n+1/2}} + \|\overrightarrow{\lambda}_{\mathrm{f}}^{n}\|_{\mathbb{M}_\Gamma}\\ &\leq \Delta t\sqrt{\frac{8}{\eta\mathrm{m}}\mathbf{E}^{1/2}} + \|\overrightarrow{\lambda}_{\mathrm{f}}^{n}\|_{\mathbb{M}_\Gamma}\\ &\leq T\sqrt{\frac{8}{\eta\mathrm{m}}\mathbf{E}^{1/2}} + \|\overrightarrow{\lambda}_{\mathrm{f}}^{0}\|_{\mathbb{M}_\Gamma}.\end{aligned} \tag{22}$$

One can resort to the same arguments to derive the corresponding estimate for the second mortar unknown

$$\|\overrightarrow{\lambda}_{\mathrm{s}}^{n+1}\|_{\mathbb{M}_\Gamma} \leq T\sqrt{\frac{8}{\eta\mathrm{s}}\mathbf{E}^{1/2}} + \|\overrightarrow{\lambda}_{\mathrm{s}}^{0}\|_{\mathbb{M}_\Gamma}. \tag{23}$$

We now move on to the volume unknowns and start with the fluid discrete propagator. From the definition (20) of the matrix $\widetilde{\mathbb{M}}_{\mathrm{f}}$ and the definition (19) of $\overline{\Delta t}$ we have

$$\forall\overrightarrow{\phi}\in\mathbb{R}^{N_{\mathrm{f}}},\quad \overline{\Delta t}^2\|\overrightarrow{\phi}\|_{\widetilde{\mathbb{M}}_{\mathrm{f}}}^2 = \overline{\Delta t}^2\|\overrightarrow{\phi}\|_{\mathbb{M}_{\mathrm{f}}}^2 - \Delta t^2\frac{\overline{\Delta t}^2}{4}\|\overrightarrow{\phi}\|_{\mathbb{K}_{\mathrm{f}}}^2 \geq (\overline{\Delta t}^2 - \Delta t^2)\|\overrightarrow{\phi}\|_{\mathbb{M}_{\mathrm{f}}}^2.$$

As previously, we invoke Lemma 6 to insure that the total discrete energy is the sum of positive functionals and derive the following estimate

$$\Big\|\frac{\overrightarrow{\phi}^{n+1}-\overrightarrow{\phi}^{n}}{\Delta t}\Big\|_{\mathbb{M}_{\mathrm{f}}}^2 \leq \frac{\overline{\Delta t}^2}{(\overline{\Delta t}^2-\Delta t^2)}\Big\|\frac{\overrightarrow{\phi}^{n+1}-\overrightarrow{\phi}^{n}}{\Delta t}\Big\|_{\widetilde{\mathbb{M}}_{\mathrm{f}}}^2 \leq \frac{2\overline{\Delta t}^2}{(\overline{\Delta t}^2-\Delta t^2)}\mathbf{E}^{n+1/2}.$$

Hence, due to the conservation of the fully discrete energy one has

$$\|\overrightarrow{\phi}^{n+1}\|_{\mathbb{M}_{\mathrm{f}}} \leq \Delta t\Big\|\frac{\overrightarrow{\phi}^{n+1}-\overrightarrow{\phi}^{n}}{\Delta t}\Big\|_{\mathbb{M}_{\mathrm{f}}} + \|\overrightarrow{\phi}^{n}\|_{\mathbb{M}_{\mathrm{f}}} \leq \frac{T\sqrt{2}\,\overline{\Delta t}}{(\overline{\Delta t}^2-\Delta t^2)^{1/2}}\sqrt{\mathbf{E}^{1/2}} + \|\overrightarrow{\phi}^{0}\|_{\mathbb{M}_{\mathrm{f}}}. \tag{24}$$

Following the same line of arguments we have the corresponding upper bound on the volume unknowns of the solid discrete propagator, namely

$$\|\overrightarrow{u}^{n+1}\|_{\mathbb{M}_{\mathrm{s}}} \leq \frac{T\sqrt{2}\,\overline{\Delta t}}{(\overline{\Delta t}^2-\Delta t^2)^{1/2}}\sqrt{\mathbf{E}^{1/2}} + \|\overrightarrow{u}^{0}\|_{\mathbb{M}_{\mathrm{s}}}. \tag{25}$$

Finally, combining the results (22), (23), (24), and (25), we obtain the stability result (21) with

$$C_0 = \Big(\frac{2\sqrt{2}\,\overline{\Delta t}}{(\overline{\Delta t}^2-\Delta t^2)^{1/2}} + \sqrt{\frac{8}{\eta\mathrm{m}}} + \sqrt{\frac{8}{\eta\mathrm{s}}}\Big)T\sqrt{\mathbf{E}^{1/2}} + \|\overrightarrow{\phi}^{0}\|_{\mathbb{M}_{\mathrm{f}}} + \|\overrightarrow{u}^{0}\|_{\mathbb{M}_{\mathrm{s}}} + \|\overrightarrow{\lambda}_{\mathrm{f}}^{0}\|_{\mathbb{M}_\Gamma} + \|\overrightarrow{\lambda}_{\mathrm{s}}^{0}\|_{\mathbb{M}_\Gamma}. \tag{26}$$

□

From the previous stability result we can deduce the well-posedness of (16), which has not intent but to insure that the choice of our mortar unknowns is relevant, and that it leads to a sound fully-discrete scheme.

Corollary 1. *For any step index $n \geq 1$, we denote by $N_S = 2(N_\mathrm{f} + N_\mathrm{s} + 2N_\Gamma)$ and by*

$$\overrightarrow{S}^n = \begin{pmatrix} \overrightarrow{\phi}^n & \overrightarrow{u}^n & \overrightarrow{\lambda}_\mathrm{f}^n & \overrightarrow{\lambda}_\mathrm{s}^n & \overrightarrow{\phi}^{n-1} & \overrightarrow{u}^{n-1} & \overrightarrow{\lambda}_\mathrm{f}^{n-1} & \overrightarrow{\lambda}_\mathrm{s}^{n-1} \end{pmatrix}^\intercal \in \mathbb{R}^{N_S}$$

the state vector associated to the discrete dynamics (16)*. Assuming that $\Delta t < \overline{\Delta t}$, the transition operator $\mathbb{T}_{n|1}$*

$$\begin{array}{rccc} \mathbb{T}_{n|1} & : & \mathbb{R}^{N_S} & \mapsto & \mathbb{R}^{N_S} \\ & & \overrightarrow{S}^1 & \to & \overrightarrow{S}^n \end{array}$$

which, from a known initial state $\overrightarrow{S}^1$, gives the state $\overrightarrow{S}^n$ obtained by performing the iterations (16) *up to the step index n, is an invertible linear operator. In general, for any positive index k the transition operator $\mathbb{T}_{n+k|n}$ is invertible.*

Proof. The linearity of the transition operator is straightforward. Let us consider two states generated by the same initial conditions and their difference, namely

$$\forall n \geq 1, \quad \overrightarrow{R}^n = \mathbb{T}_{n|1}\,\overrightarrow{S}^1, \quad \overrightarrow{S}^n = \mathbb{T}_{n|1}\,\overrightarrow{S}^1, \quad \text{and} \quad \overrightarrow{\delta S}^n = \overrightarrow{R}^n - \overrightarrow{S}^n.$$

By linearity, $\overrightarrow{\delta S}^n$ is generated from a null initial state. Hence, using the stability result (21), and more specifically the dependency (26) of the stability constant *w.r.t.* the initial conditions, we can insure that $\overrightarrow{S}^n = \overrightarrow{R}^n$. Therefore, the transition operator is an injective operator on a finite dimensional space, which, by the rank-nullity theorem, is equivalent to being invertible. Using the same arguments, one can extend this property to $\mathbb{T}_{n+k|n}$. □

3.5. Time marching algorithm

In order to provide a more practical description of the time marching algorithm associated to the fully discrete scheme (16) – and to detail the operations to be performed at each time step – we regroup the volume unknowns and interface unknowns in the following manner

$$\overrightarrow{X}^n = \begin{pmatrix} \overrightarrow{\phi}^n & \overrightarrow{u}^n \end{pmatrix}^\intercal \in \mathbb{R}^{N_\mathrm{f}+N_\mathrm{s}}, \quad \overrightarrow{L}^n = \begin{pmatrix} \overrightarrow{\lambda}_\mathrm{f}^n & \overrightarrow{\lambda}_\mathrm{s}^n \end{pmatrix}^\intercal \in \mathbb{R}^{2N_\Gamma}.$$

With this notation, the discrete scheme (16) can be recast in the following form

$$\begin{pmatrix} \mathbb{A} & \mathbb{B} \\ \mathbb{C}^\intercal & \mathbb{D} \end{pmatrix} \begin{pmatrix} \overrightarrow{X}^{n+1} \\ \overrightarrow{L}^{n+1} \end{pmatrix} = \begin{pmatrix} \overrightarrow{F} + \mathbb{B}\overrightarrow{L}^{n-1} \\ \overrightarrow{G} \end{pmatrix}, \tag{27}$$

where the block matrices are given by

$$\mathbb{A} = \begin{pmatrix} \mathbb{M}_\mathrm{f} & \\ & \mathbb{M}_\mathrm{s} \end{pmatrix}, \ \mathbb{B} = \tfrac{\Delta t}{2} \begin{pmatrix} \mathbb{C}_\mathrm{f} & \\ & -\mathbb{C}_\mathrm{s} \end{pmatrix}, \ \mathbb{C}^\intercal = \tfrac{1}{2} \begin{pmatrix} -\mathbb{C}_\mathrm{f}^\intercal & \frac{\eta_\mathrm{m}}{\Delta t}\mathbb{C}_\mathrm{s}^\intercal \\ \frac{\eta_\mathrm{s}}{\Delta t}\mathbb{C}_\mathrm{f}^\intercal & \mathbb{C}_\mathrm{s}^\intercal \end{pmatrix}, \ \mathbb{D} = \tfrac{1}{2} \begin{pmatrix} \frac{\eta_\mathrm{m}}{\Delta t}\mathbb{M}_\Gamma & \mathbb{M}_\Gamma \\ -\mathbb{M}_\Gamma & \frac{\eta_\mathrm{s}}{\Delta t}\mathbb{M}_\Gamma \end{pmatrix},$$

and the right-hand sides are

$$\overrightarrow{F} = \begin{pmatrix} -\Delta t^2 \mathbb{K}_\mathrm{f}\,\overrightarrow{\phi}^n + \mathbb{M}_\mathrm{f}\big(2\overrightarrow{\phi}^n - \overrightarrow{\phi}^{n-1}\big) \\ -\Delta t^2 \mathbb{K}_\mathrm{s}\,\overrightarrow{u}^n + \mathbb{M}_\mathrm{s}\big(2\overrightarrow{u}^n - \overrightarrow{u}^{n-1}\big) \end{pmatrix}, \ \overrightarrow{G} = \begin{pmatrix} \frac{1}{2}\mathbb{C}_\mathrm{f}^\intercal\,\overrightarrow{\phi}^n + \frac{\eta_\mathrm{m}}{2\Delta t}\mathbb{C}_\mathrm{s}^\intercal\,\overrightarrow{u}^n + \frac{\eta_\mathrm{m}}{2\Delta t}\mathbb{M}_\Gamma\,\overrightarrow{\lambda}_\mathrm{f}^n - \frac{1}{2}\mathbb{M}_\Gamma\,\overrightarrow{\lambda}_\mathrm{s}^n \\ \frac{\eta_\mathrm{s}}{2\Delta t}\mathbb{C}_\mathrm{f}^\intercal\,\overrightarrow{\phi}^n - \frac{1}{2}\mathbb{C}_\mathrm{s}^\intercal\,\overrightarrow{u}^n + \frac{1}{2}\mathbb{M}_\Gamma\,\overrightarrow{\lambda}_\mathrm{f}^n + \frac{\eta_\mathrm{s}}{2\Delta t}\mathbb{M}_\Gamma\,\overrightarrow{\lambda}_\mathrm{s}^n \end{pmatrix}.$$

Introducing the Schur complement matrix

$$\mathbb{S} = \mathbb{D} - \mathbb{C}^\intercal \mathbb{A}^{-1} \mathbb{B}, \tag{28}$$

the solution of the linear system (27) is given by the following relations

$$\begin{cases} \overrightarrow{L}^{n+1} = \mathbb{S}^{-1}\big(\overrightarrow{G} - \mathbb{C}^\intercal \mathbb{A}^{-1}(\overrightarrow{F} + \mathbb{B}\,\overrightarrow{L}^{n-1})\big), \\ \overrightarrow{X}^{n+1} = \mathbb{A}^{-1}\big(\overrightarrow{F} + \mathbb{B}(\overrightarrow{L}^{n-1} - \overrightarrow{L}^{n+1})\big). \end{cases}$$

From this form of (27), one can derive an algorithm more suitable for computer implementation. Let $\overrightarrow{X}^* \in \mathbb{R}^{N_\mathrm{f}+N_\mathrm{s}}$ be an auxiliary variable for volume unknowns operations, and let $\overrightarrow{X}^n$, $\overrightarrow{X}^{n-1}$ and $\overrightarrow{L}^n$ be the previously computed solution steps, then the solution of (27) can be obtained through the following operations:

$$\begin{aligned} &1 - \textbf{Propagators pre-process step:} && \overrightarrow{X}^* \leftarrow \overrightarrow{F}, \\ &2 - \textbf{Interface pre-process step:} && \overrightarrow{X}^* \leftarrow \overrightarrow{X}^* + \mathbb{B}\,\overrightarrow{L}^{n-1}, \\ &3 - \textbf{Propagators compute step:} && \overrightarrow{X}^* \leftarrow \mathbb{A}^{-1}\overrightarrow{X}^*, \\ &4 - \textbf{Interface compute step:} && \overrightarrow{L}^{n+1} \leftarrow \mathbb{S}^{-1}\big(\overrightarrow{G} - \mathbb{C}^\intercal \overrightarrow{X}^*\big), \\ &5 - \textbf{Propagators post-process step:} && \overrightarrow{X}^{n+1} \leftarrow \overrightarrow{X}^* - \mathbb{A}^{-1}\mathbb{B}\,\overrightarrow{L}^{n+1}. \end{aligned} \tag{29}$$

3.6. Analysis of the Schur complement matrix

After mass lumping (see Section 3.1) the matrix $\mathbb{A}$ is diagonal. Hence, in terms of performances, the remaining issue is the treatment of the Schur complement matrix $\mathbb{S}$, that needs to be inverted in the interface compute step. The goal of this section is to give some further details on the structure of this matrix. To start with, we give the following well-posedness result.

Property 1. *Assuming that $\Delta t < \overline{\Delta t}$, the Schur complement matrix $\mathbb{S}$ defined in* (28) *is invertible.*

Proof. By virtue of Corollary 1, the matrix appearing in system (27) is invertible. Since the matrix $\mathbb{A}$ is also invertible, so is the Schur complement matrix. □

Property 2. *Inverting the Schur complement matrix – of size $2N_\Gamma \times 2N_\Gamma$ – can be reduced to inverting a matrix of size $N_\Gamma \times N_\Gamma$ only.*

Proof. The Schur complement matrix can be expressed in block form as

$$\mathbb{S} = \begin{pmatrix} \mathbb{S}_{11} & \mathbb{S}_{12} \\ \mathbb{S}_{21} & \mathbb{S}_{22} \end{pmatrix} = \begin{pmatrix} \frac{\eta^\mathrm{m}}{2\Delta t}\mathbb{M}_\Gamma + \frac{\Delta t}{4}\mathbb{C}_\mathrm{f}^\intercal \mathbb{M}_\mathrm{f}^{-1}\mathbb{C}_\mathrm{f} & \frac{1}{2}\mathbb{M}_\Gamma + \frac{\eta^\mathrm{m}}{4}\mathbb{C}_\mathrm{s}^\intercal \mathbb{M}_\mathrm{s}^{-1}\mathbb{C}_\mathrm{s} \\ -\frac{1}{2}\mathbb{M}_\Gamma - \frac{\eta^\mathrm{s}}{4}\mathbb{C}_\mathrm{f}^\intercal \mathbb{M}_\mathrm{f}^{-1}\mathbb{C}_\mathrm{f} & \frac{\eta^\mathrm{s}}{2\Delta t}\mathbb{M}_\Gamma + \frac{\Delta t}{4}\mathbb{C}_\mathrm{s}^\intercal \mathbb{M}_\mathrm{s}^{-1}\mathbb{C}_\mathrm{s} \end{pmatrix}.$$

Therefore, the solution of the linear systems of the following nature:

$$\text{for a given } \overrightarrow{b} = \big(\overrightarrow{b_\mathrm{f}}\ \overrightarrow{b_\mathrm{s}}\big)^\intercal \in \mathbb{R}^{2N_\Gamma}, \text{ find } \overrightarrow{\lambda}^* = \big(\overrightarrow{\lambda}_\mathrm{f}^*\ \overrightarrow{\lambda}_\mathrm{s}^*\big)^\intercal \in \mathbb{R}^{2N_\Gamma}, \text{ such that } \mathbb{S}\,\overrightarrow{\lambda}^* = \overrightarrow{b},$$

are given by

$$\overrightarrow{\lambda}_\mathrm{f}^* = \big(\mathbb{S}_{11} - \mathbb{S}_{12}\mathbb{S}_{22}^{-1}\mathbb{S}_{21}\big)^{-1}\big(\overrightarrow{b_\mathrm{f}} - \mathbb{S}_{12}\mathbb{S}_{22}^{-1}\overrightarrow{b_\mathrm{s}}\big), \quad \overrightarrow{\lambda}_\mathrm{s}^* = \mathbb{S}_{22}^{-1}\big(\overrightarrow{b_\mathrm{s}} - \mathbb{S}_{21}\,\overrightarrow{\lambda}_\mathrm{f}^*\big). \tag{30}$$

The block $\mathbb{S}_{22}$ is positive definite and – according to Lemma 4 – diagonal (with trivial inverse). Therefore, the only matrix to be inverted is

$$\begin{aligned} \mathbb{S}_{11} - \mathbb{S}_{12}\mathbb{S}_{22}^{-1}\mathbb{S}_{21} = \tfrac{\eta^\mathrm{m}}{2\Delta t}\mathbb{M}_\Gamma + \tfrac{\Delta t}{4}\mathbb{C}_\mathrm{f}^\intercal \mathbb{M}_\mathrm{f}^{-1}\mathbb{C}_\mathrm{f} \\ + \big(\tfrac{1}{2}\mathbb{M}_\Gamma + \tfrac{\eta^\mathrm{m}}{4}\mathbb{C}_\mathrm{s}^\intercal \mathbb{M}_\mathrm{s}^{-1}\mathbb{C}_\mathrm{s}\big)\big(\tfrac{\eta^\mathrm{s}}{2\Delta t}\mathbb{M}_\Gamma + \tfrac{\Delta t}{4}\mathbb{C}_\mathrm{s}^\intercal \mathbb{M}_\mathrm{s}^{-1}\mathbb{C}_\mathrm{s}\big)^{-1}\big(\tfrac{1}{2}\mathbb{M}_\Gamma + \tfrac{\eta^\mathrm{s}}{4}\mathbb{C}_\mathrm{f}^\intercal \mathbb{M}_\mathrm{f}^{-1}\mathbb{C}_\mathrm{f}\big). \end{aligned}$$

Note that, since both the Schur complement matrix and the block $\mathbb{S}_{22}$ are invertible, this matrix is necessarily invertible. □

Property 3. *In the case of a conform interface the discrete scheme* (16) *is fully explicit.*

Proof. Upon the conform interface assumption, using Lemma 4, the matrix $\mathbb{S}_{11} - \mathbb{S}_{12}\mathbb{S}_{22}^{-1}\mathbb{S}_{21}$ is diagonal. Hence the solution defined in (30) is obtained by simply applying the inverse of diagonal matrices. Since the matrix $\mathbb{A}$ is also diagonal, the steps described in (29) and carried out at each time increment do not require solving a linear system. □

Remark 4. *The propagators pre-process and compute steps – i.e. steps* 1 *and* 3 *in* (29) *– are exactly the same as performed without an interface. This has an important impact in terms of computer implementation, since it clearly shows the decomposition between the volume operations (steps* 1 *and* 3*) and the interface operations (steps* 2*,* 4 *and* 5*).*

4. Numerical illustrations

4.1. Computational loads associated to the reference, the ETC conform and the ETC non-conform schemes

In this section we aim at illustrating the gain in terms of computational performances obtained by our approach. To do so, we use as "Reference" the standard explicit time scheme with a meshed coating layer (*i.e.* without ETC) and conform space discretizations at the interface. As a first comparison step, we consider the "ETC conform" case where the coating layer is represented through effective transmissions and the mesh for the fluid domain and the solid domain are conform at the interface. As a final comparison step, we consider the "ETC non-conform" case where the coating layer is also represented through ETCs but the meshes are different at the interface. In order to better understand the computational loads associated to each scheme, we recall their main characteristics:

— **Reference**: The three domains Ω_f, Ω_s, and Ω^η are meshed. We apply an explicit leap frog scheme with mass lumping for each domains. The fluid – solid interface between Ω_f and Ω^η is also treated using the mortar method as detailed in [15]. Since the meshes are conform at the interface, the obtained Schur matrix can be lumped so that the overall scheme is fully explicit. In this context, the main computation load for each propagator resides in the application of the stiffness matrix onto an input finite element vector. Following [15] this operation is applied element-wise, in parallel, in a unassembled manner. Note that, in this case, the stability condition of the overall discrete scheme is necessarily proportionate to η, and the solid domain is potentially over discretized because of the conformity constraint at the interface.

— **ETC conform**: Only Ω_f and Ω_s are meshed and the contribution of the coating layer is incorporated using effective transmissions. Each propagator supports an explicit leap frog scheme with mass lumping. Hence, the step 3 in (29) exclusively implies diagonal matrices, and can be carried out very efficiently. Additionally, the stiffness operations are performed element-wise in parallel, as for the reference case. The interface between Ω_f and Ω_s is conform. In virtue of Property 3, the Schur complement matrix in step 4 of (29) is lumped, and this step bears little computational load. Additionally, thanks to Theorem 1 we can insure that the CFL condition of the complete scheme is independent of the layer thickness or its effective parameters. However, as a potential drawback, the solid domain is potentially over discretized in order to satisfy the conformity constraint.

— **ETC non-conform**: As for the previous case, only Ω_f and Ω_s are meshed and we use ETCs to represent the coating layer. Each propagator are identical to the previous case, and the CFL condition is also independent of the coating layer effective parameters. However, in this case we suppress the conformity constraint, hoping to limit the computational load associated to the solid domain by reducing the associated number of degrees of freedom. The price to pay for this non-conform case is a non-diagonal Schur complement matrix. We have to solve at each time step the linear system appearing in step 4 of (29). In practice, since this matrix is constant over time, we compute its LU factorization in an initializing phase, and perform the forward and backward substitutions at each iteration.

4.2. Illustration of performances for a 2D configuration

Let us start with a simple 2D case. The fluid domain is composed of water and the solid domain is steel material, namely

$$\rho_{\mathrm{f}} = 1.0\,\mathrm{g}\cdot\mathrm{cm}^{-3},\ c = 1.5\,\mathrm{mm}\cdot\mu\mathrm{s}^{-1},\ \rho_{\mathrm{s}} = 8.0\,\mathrm{g}\cdot\mathrm{cm}^{-3},\ \lambda = 144\,\mathrm{GPa},\ \mu = 72\,\mathrm{GPa}.$$

The support of the initial condition ϕ_0 corresponds to a regularized line source calibrated in order to generate a wide band wave packet centered at 1.0 MHz. At this frequency the pressure wavelength in the fluid and the shear and pressure wavelengths in the solid are respectively

$$\lambda_P^{\mathrm{f}} = 1.5\,\mathrm{mm},\quad \lambda_S^{\mathrm{s}} = 3.0\,\mathrm{mm},\quad \lambda_P^{\mathrm{s}} = 6.0\,\mathrm{mm},\qquad i.e.\qquad \lambda_P^{\mathrm{f}} = \frac{\lambda_S^{\mathrm{s}}}{2} = \frac{\lambda_P^{\mathrm{s}}}{4}.$$

The size of the domains are chosen to be proportionate to the pressure wavelengths, in particular the fluid domain is the square $25\lambda_P^{\mathrm{f}} \times 25\lambda_P^{\mathrm{f}}$, while the solid domain is the rectangle $25\lambda_P^{\mathrm{f}} \times 25\lambda_P^{\mathrm{s}}$. The thickness of the coating layer is set to be $\eta = \lambda_P^{\mathrm{f}}/10$ and the material of the layer is twice as stiff as the solid domain, *i.e.*

$$\rho' = \rho_{\mathrm{s}},\ \lambda' = 2\lambda,\ \mu' = 2\mu,$$

from which we can derive the effective transmission coefficients using (10). Concerning the discretization parameter we use spectral elements of order five with three elements per λ_P^{f} in the fluid domain. For the solid domain we consider both cases of conform discretization (where we impose the same discretization as the fluid domain) and non-conform discretization where the order remains five but we set three elements per λ_S^{s}, leading to $H = 2h$. We carry out numerical simulations by computing the upper bound on the time step provided in (19).

In Table 1 we regroupe the various computational characteristics of the different schemes: the reference simulation (*i.e.* standard explicit scheme with meshed coating layer) compared with both cases of ETC with conform and non-conform interface. In terms of degrees of freedom the reference and the case of conform ETC are similar (the only difference lies in the number of DoFs in the coating layer), while for the non-conform case we have an important drop, which is due to the space discretization being more coarse in the solid domain. In terms of time step, we also have a gain in the conform ETC case, due to the fact the time scheme is independent of the coating layer thickness. In the non-conform ETC case the gain in time step is even larger. Combining both positive effects we observe a significant improvement of a factor more than $\times 15$ for the non-conform with ETC case.

	No ETC	ETC conform		ETC non-conform	
			·/ref.		·/ref.
Number of DoFs	$395 \cdot 10^3$	$392 \cdot 10^3$	$1/1.007$	$242 \cdot 10^3$	$1/1.63$
Timestep Δt (μs)	$1.59 \cdot 10^{-3}$	$9.12 \cdot 10^{-3}$	5.73	$15.94 \cdot 10^{-3}$	9.74
CPU Time* per iter. (s)	$5.39 \cdot 10^{-3}$	$5.39 \cdot 10^{-3}$	1.0	$3.53 \cdot 10^{-3}$	$1/1.53$
CPU Time* (s)	168	30	$1/5.6$	11	$1/15.3$

Table 1: Table regrouping the computational characteristics of the different schemes for the 2D configuration. **computations performed on a laptop PC, Intel(R) Core(TM) i7-8850H CPU @ 2.60 GHz.*

In Figure 2 we represent snapshots of the solutions at three different time values. In these snapshots we can see a very good agreement when comparing reflected pressure wave in the fluid and bulk waves in the solid (both pressure and transverse waves). We observe some discrepancies for the surface waves. These discrepancies appear even in the conform case, implying that the ETC cannot adequately capture these contributions.

To better validate the proposed numerical scheme we propose in Figure 3 to extract over time the y component of the solution at three observation points. As depicted in Figure 2, we position a first point

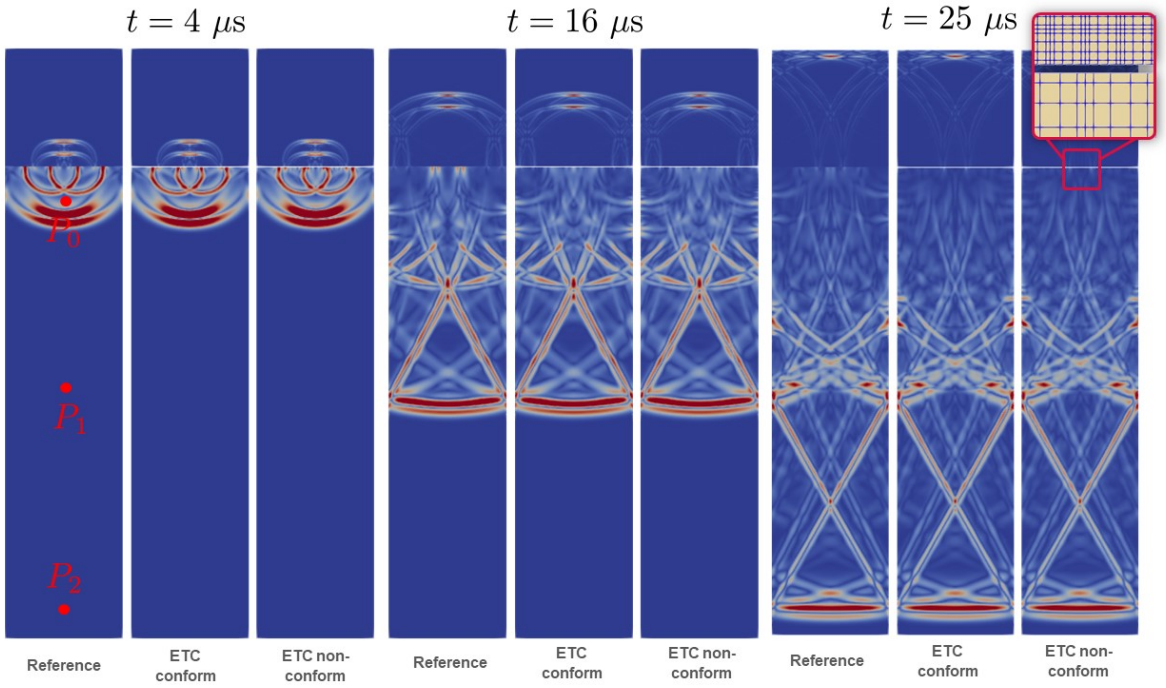

Figure 2: Illustration and snapshots of the solutions. On the top right we illustrate the mesh non-conformity at the fluid – solid interface, also depicted in Figure 1 and corresponds to $H = 2h$ and $p = q = 5$. Red dots represent the position of the observation points.

near the interface, a second point in the middle of the solid domain and a third point far from the interface. Even though the time step for each discretization is different, we observe a very good agreement between the three numerical solutions, with once again some discrepancies at the observation point located near the interface. To better illustrate these discrepancies we show in Figure 4 a zoom of the extracted solution in the time interval $[15\,\mu s; 25\,\mu s]$.

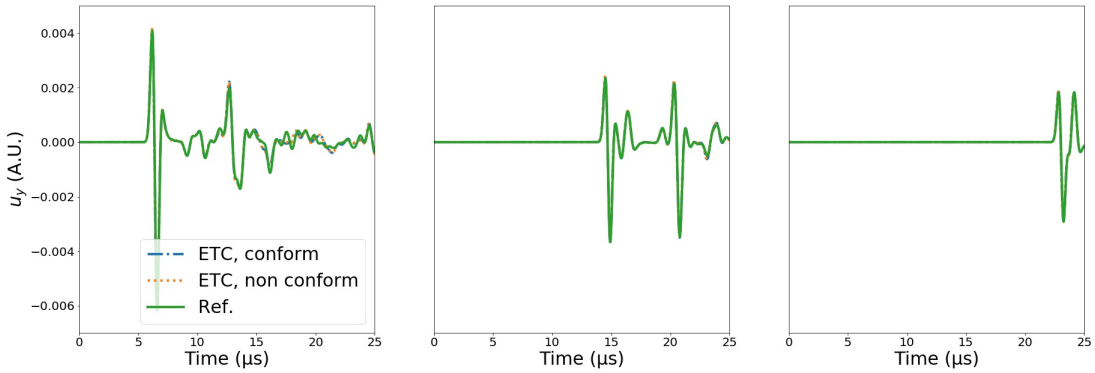

Figure 3: Comparing the time variation of the solutions at the observation points P_0 (left), P_1 (middle) and P_2 (right) for the 2D configuration.

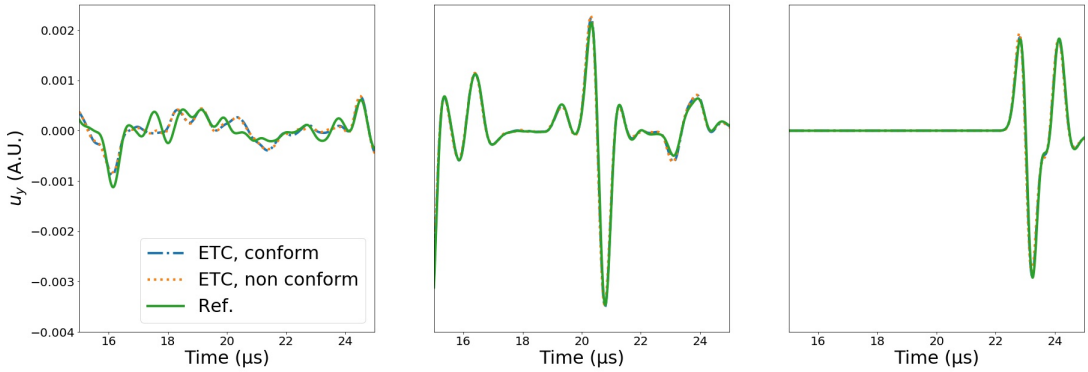

Figure 4: Comparing the time variation of the solutions at the observation points P_0 (left), P_1 (middle) and P_2 (right) for the 2D configuration with a focus on the interval time $[15\,\mu s; 25\,\mu s]$.

4.3. Illustration of energy conservation

From the previous numerical example of the performance gain one can obtain from combining ETC with a non-conform interface, we can also compute the energies (kinetic and potential) associated to each propagator, namely fluid and solid, along with the energies associated to the interface. In practice, we use the expressions provided in the energy conservation Lemma 5 to compute the components of the total energy. In Figure 5 we show the evolution of the total energy (and its various components) in time, in addition with its time-discrete derivative. These plots clearly illustrate the conservation property as the total energy remains constant over the time window. In particular, the magnitude of the time-derivative of the total fully discrete energy is of 10^{-11}, variations that can be attributed to spurious numerical contributions. In Figure 6 we plot the different terms of the total energy. We can clearly observe the time variations of individual components of the total energy, that are – after summation – perfectly balanced so that the conservation property is satisfied. For the fluid propagator, we observe exchanges between kinetic and potential energies, specifically at initial times and after rebound on the upper boundary. For the solid propagator, one can remark the increasing trend due to the transfer of the wave packet from the fluid domain to the solid domain. At similar times, when the wave packet travel through the interface, we observe an expected increase in the energy terms associated to the ETCs.

4.4. Illustration of space convergence

Even though the previous numerical example shows a very good agreement between the proposed approach (with or without non-conformity) and the reference solution, an important question is whether or not the introduction of the mortar unknowns degrades the space convergence of the discrete fluid and solid propagators. In order to address this question, we propose in this section to compute convergence curves for both cases of ETCs with conform and non-conform interface. Since we are dealing with time varying discrete solutions, we need to compute time – space convergence curves. In particular, we choose the popular "$L^\infty - L^2$" relative error. More precisely, for the given mesh steps h and H, we compute

$$e_{\mathrm{f}} = \frac{\sup_n \|\phi^\star(t^n) - \phi_h^n\|_{L^2(\Omega_{\mathrm{f}})}}{\sup_n \|\phi^\star(t^n)\|_{L^2(\Omega_{\mathrm{f}})}}, \qquad e_{\mathrm{s}} = \frac{\sup_n \|\mathbf{u}^\star(t^n) - \mathbf{u}_H^n\|_{L^2(\Omega_{\mathrm{s}})^3}}{\sup_n \|\mathbf{u}^\star(t^n)\|_{L^2(\Omega_{\mathrm{s}})^3}},$$

for the fluid and solid propagators respectively. In these expressions, $\phi^\star$ and $\mathbf{u}^\star$ are reference solutions obtained using the same numerical algorithm with a much refined mesh – with a mesh step denoted by $h^\star$. From the well-known standard *a priori* error estimations – see *e.g.* [23] – we expect to have $e_{\mathrm{f}} = O(\Delta t^2 + h^{p+1})$ and $e_{\mathrm{s}} = O(\Delta t^2 + H^{q+1})$, showing that these convergence curves include both time and space discretization errors. Since we are mainly focused on the effect of the mortar interface on the space

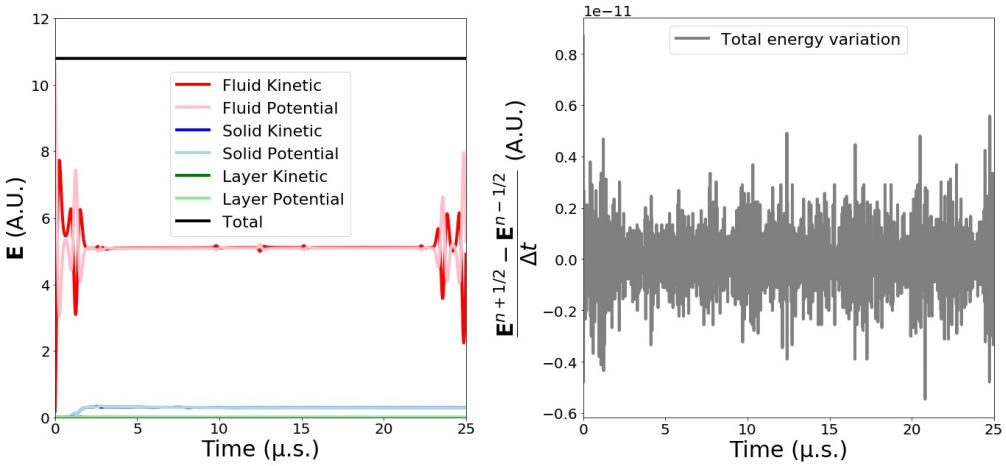

(a) Total energy (b) Energy time variation

Figure 5: Total energy over time and its discrete time derivative of the fully discrete scheme in the non-conform ETC case. Note that the overall scale of the plot for the time variation is 10^{-11}, showing the energy conservation property over the time window.

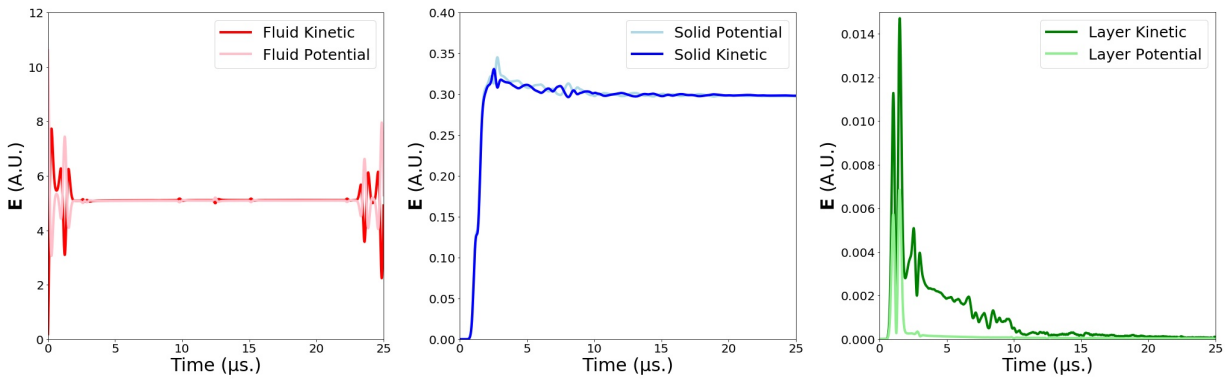

(a) Fluid energies (b) solid energies (c) Layer energies

Figure 6: Kinetic and potential energies associated to the fluid, solid and ETC layer unknowns over time for the non-conform ETC case.

convergence, we impose for each convergence points – and regardless of the mesh step – a refined time step of $\Delta t^\star$. In practice, we take the time step used to obtain the reference solutions $\phi^\star$ and $\mathbf{u}^\star$. By doing so, we exclude any time interpolation error when computing e_f and e_s, and we can assume that the main contribution to these errors comes from the space discretization.

The configuration parameters are identical to the one prescribed in the previous sections expect that, in order to reduce the computation times, we choose a smaller solid domain of size $25\lambda_P^\mathrm{f} \times 25\lambda_P^\mathrm{f}$. The mesh step in the fluid domain varies as $h \in \{3.75, 1.875, 0.9375, 0.46875\}$ mm, and we impose $H = h$ for the ETC conform case and $H = 2h$ for the ETC non-conform case. The reference mesh steps are set to $h^\star = 0.1171875$ mm for the fluid domain, and $H^\star = h^\star$ or $H^\star = 2h^\star$ for the conform and non-conform case respectively. The order of approximation in both the conform and non-conform case are identical in the fluid and solid domain, *i.e.* $p = q$, and we consider three cases $p \in \{1, 2, 3\}$. For the different values of p, we give the time step used in the computations of the convergence curves, *i.e.* the reference time step $\Delta t^\star$ in Table 2. Note that they are obtained from the CFL condition (19). Finally, in order to limit the influence

of the interpolation error of the initial condition we choose a smoother function ϕ^0 by defining

$$\forall \mathbf{x} \in \Omega_{\mathrm{f}}, \quad \phi^0(\mathbf{x}) = \exp\Big(- \frac{\|\mathbf{x} - \mathbf{x}_0\|_2^2}{\sigma_0^2} \Big), \quad \mathbf{x}_0 = (18.75, 57.5)^\intercal, \quad \sigma_0 = 3.5 \text{ mm}.$$

p, order of approx.	1	2	3
$\Delta t^\star$, ETC conform (μs)	0.0156	0.0061	0.0033
$\Delta t^\star$, ETC non-conform (μs)	0.0313	0.0122	0.0066

Table 2: Table regrouping the various reference time steps used to compute the convergence curves in Figure 7.

The convergence curves are presented in Figure 7. We plot the evolution of the relative errors e_{f} and e_{s} for the fluid (left plot) and the solid (right plot) respectively. For the fluid case, we remark that the curves for the conform and non-conform cases are very similar. Their differences are small enough to obtain superposing curves. Additionally, we obtain the expected convergence rates of $O(h^{p+1})$. For the solid case, since the mesh steps in the conform and non-conform cases are different, the curves cannot be superposed. However, we obtain the expected convergence rates of $O(H^{p+1})$. Hence, these convergence curves illustrate the fact that the use of a mortar interface with ETC conditions does not seem to degrade or modify the space convergence of the discrete fluid and solid propagators.

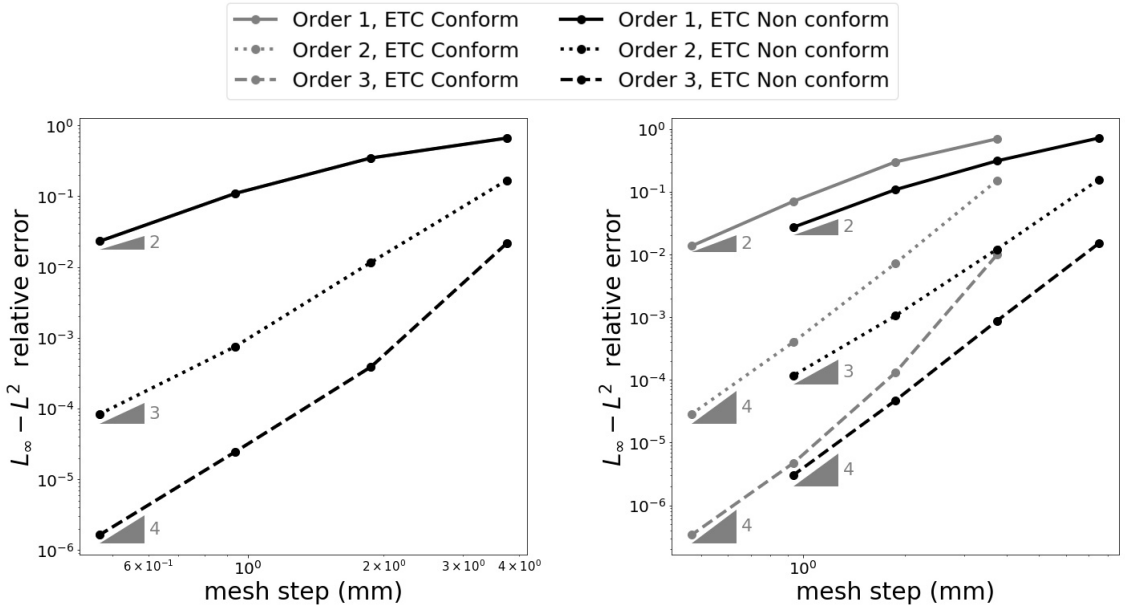

(b) Fluid relative error e_{f}

(c) Solid relative error e_{s}

Figure 7: Time – space convergence curves for the fluid (left) and solid (right) propagators, and for the ETC conform case and the ETC non-conform case in 2D. In order to emphasize space convergence, the time step for each points in the curves is $\Delta t^\star$, the time step used to obtain reference solution.

4.5. Illustration of performances for a 3D configuration

We extend the previous result to a 3D configuration where in the out-of-plane direction the domains are extended by a length of $25\lambda_P^{\mathrm{f}}$. The rest of the parameters presented in Section 4.2 are identical.

We show in Table 3 the various computational characteristics of the simulation. In terms of number of DoFs, as expected, the non-conformity allows us to drastically reduce the number of space discretization points in the solid domain. Additionally, the time step allowed by the CFL condition is up to eight times

	No ETC	ETC conform		ETC non-conform	
			·/ref.		·/ref.
Number of DoFs	$165 \cdot 10^6$	$163 \cdot 10^6$	$1/1.008$	$61.5 \cdot 10^6$	$1/1.46$
Timestep Δt (μs)	$1.57 \cdot 10^{-3}$	$7.16 \cdot 10^{-3}$	4.56	$13.1 \cdot 10^{-3}$	8.34
CPU Time* per iter. (s)	1.385	1.329	$1/1.04$	0.666	$1/2.07$
CPU Time* (s)	$22.1 \cdot 10^3$	$4.78 \cdot 10^3$	$1/4.62$	$1.32 \cdot 10^3$	$1/16.7$

Table 3: Table regrouping the various computational characteristics of the different schemes for the 3D configuration. **computations performed on a laptop PC, Intel(R) Core(TM) i7-8850H CPU @ 2.60 GHz.*

larger for the non-conform ETC case. Even though a linear system of size proportionate to the number of DoFs at the interface must be solved at each iteration, we increase the performances of a factor more than 16 for this case.

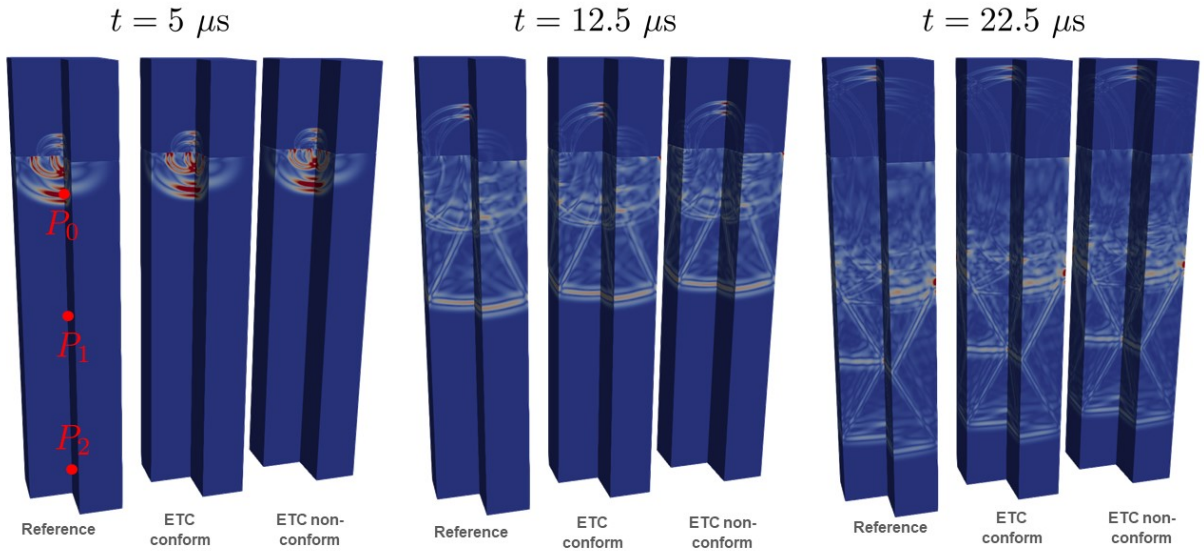

Figure 8: Illustration and snapshots of the solutions for the 3D configurations (visualizations are voluntarily cut in order to provide more insights of the various wave contributions propagating in the volumes).

In Figure 8, we present three snapshots at different time values. As for the 2D case, the bulk waves are adequately represented by the ETC cases (with conform or non-conform interface) and we observe some differences near the interface where surface waves are generated. Finally in Figure 9 we propose to extract the z component of the solution at three observation points with centered $xy-$coordinates *w.r.t* the solid domain and located along the $z-$axis close to the interface, in the middle of the domain and far from the interface. The position of these observation points are presented in Figure 8. Once again, the comparison of the time variations of the three solution at specific points shows a very good agreement, with a specific difference near the interface, which is essentially due to the lack of precision when representing surface waves with the type of ETC used in our work. This phenomenon is emphasized in Figure 10 where we present the same plots restricted to the time interval $[15\,\mu s; 25\,\mu s]$.

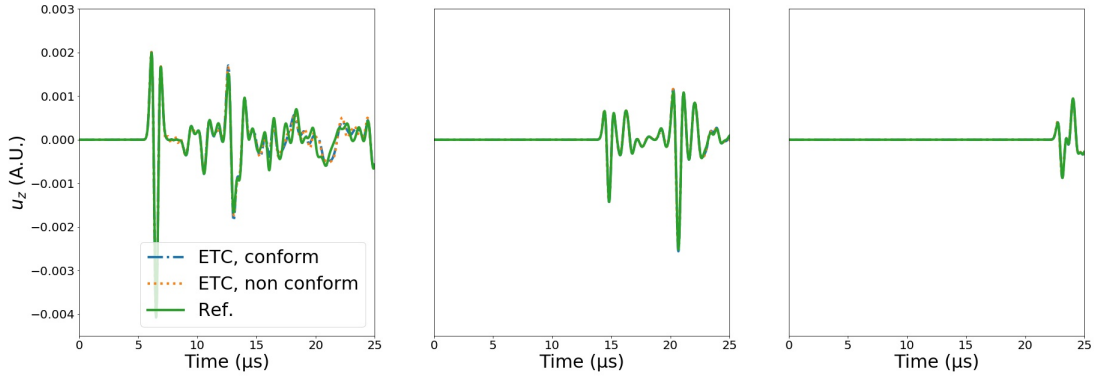

Figure 9: Comparing the time variation of the solutions the observation points P_0 (left), P_1 (middle) and P_2 (right) for the 3D configuration.

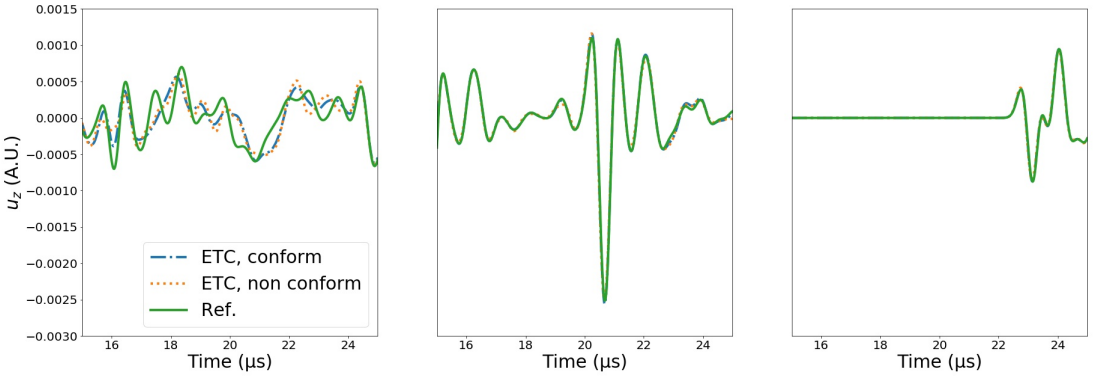

Figure 10: Comparing the time variation of the solutions the observation points P_0 (left), P_1 (middle) and P_2 (right) for the 3D configuration with a focus on the interval time $[15\,\mu s; 25\,\mu s]$.

5. Conclusions and perspectives

We have presented a way to incorporate effective transmission conditions between a fluid wave propagator and a solid wave propagator using the mortar element method. This can typically be used to efficiently represent a thin layer between the fluid and solid domains. The time discretization is composed of standard explicit leap-frog schemes for the volume propagators and an implicit scheme for the dynamics satisfied by the mortar unknowns. Using the conservation property of a discrete energy functional, we were able to prove that the fully discrete scheme is stable given a CFL condition which does not depend on the layer thickness or its effective parameters. Additionally, relying on the flexibility of the mortar element method we are able to incorporate non-conform space discretizations between the fluid mesh and the solid mesh. We proposed an efficient time-marching algorithm that separates the tasks from the volume propagators and the interface dynamics. Relying on the stability analysis we were also able to prove that this algorithm is well-posed and require only one linear system – of size equals to the number of DoFs at the interface – to be solved at each time step. Combining these assets, we were able to obtain significant performance gains on relevant 2D and 3D numerical simulations, compared to a reference approach based on a standard fully explicit scheme with a meshed coating layer.

The numerical illustrations have shown that the proposed ETC fail to represent with precision the con-

tributions of the surface waves. From a modeling point of view, this could potentially be linked to the missing tangential operators that are present in more evolved ETCs – such as the one obtained through rigorous asymptotic analysis as in [12]. Hence a potential perspective of this work is to adapt it in order to incorporate these more evolved and potentially more accurate ETCs. In the same vein, a natural improvement of the presented approach would be to relax the hypothesis (1) on the interface, and to incorporate the effect of thickness variations and curvature. Alternatively, the presented approach renders a fully discrete scheme which is very robust to changes in the coating layer thickness or material parameters. Therefore, another potential perspective would be to use this scheme within an inversion loop – such as Full Waveform Inversion [28] – in order to reconstruct characteristics of surface defects, *e.g.* corrosion flaws.

References

[1] J. Chabassier, S. Imperiale, Fourth-order energy-preserving locally implicit time discretization for linear wave equations, Int. J. Numer. Methods Eng. 106 (8) (2016) 593–622.

[2] J. Chabassier, S. Imperiale, Construction and convergence analysis of conservative second order local time discretisation for linear wave equations, ESAIM: Math. Model. Numer. Anal. 55 (4) (2021) 1507–1543.

[3] F. Ben Belgacem, Y. Maday, The mortar element method for three dimensional finite elements, ESAIM: M2AM 31 (2) (1997) 289–302.

[4] B. I. Wohlmuth, A mortar finite element method using dual spaces for the Lagrange multiplier, SIAM J. Numer. Anal. 38 (3) (2000) 989–1012.

[5] P. Hauret, P. Le Tallec, A discontinuous stabilized mortar method for general 3D elastic problems, Comput. Methods in Appl. Mech. Eng. 196 (49–52) (2007) 4881–4900.

[6] J. Diaz, M. Grote, Energy Conserving Explicit Local Time Stepping for Second-Order Wave Equations, SIAM J. Sci. Comput. 31 (3) (2009) 1985–2014.

[7] M. Grote, S. Michel, S. Sauter, Stabilized leapfrog based local time-stepping method for the wave equation, Mathematics of Computation 90 (332) (2021) 2603–2643.

[8] M. J. Grote, A. Schneebeli, D. Schötzau, Discontinuous Galerkin finite element method for the wave equation, SIAM JoNA 44 (6) (2006) 2408–2431.

[9] S. I. Rokhlin, Y. J. Wang, Analysis of boundary conditions for elastic wave interaction with an interface between two solids, J. Acoust. Soc. Am. 89 (2) (1991) 503–515.

[10] B. Lombard, J. Piraux, How to incorporate the spring-mass conditions in finite-difference schemes, SIAM J. Sci. Comput. 24 (4) (2003) 1379–1407.

[11] A. Imperiale, N. Leymarie, E. Demaldent, Numerical modeling of wave propagation in anisotropic viscoelastic laminated materials in transient regime: Application to modeling ultrasonic testing of composite structures, Int. J. Numer. Methods Eng. 121 (15) (2020) 3300–3338.

[12] M. Bonnet, A. Burel, M. Duruflé, P. Joly, Effective transmission conditions for thin-layer transmission problems in elastodynamics. The case of a planar layer model, ESAIM: M2AM 50 (1) (2016) 43–75.

[13] G. Cohen, Higher-Order Numerical Methods for Transient Wave Equations, Scientific computation, Springer, 2002.

[14] W. Ostachowicz, P. Kudela, M. Krawczuk, A. Zak, Guided waves in structures for SHM: the time-domain spectral element method, John Wiley & Sons, 2011.

[15] A. Imperiale, E. Demaldent, A macro-element strategy based upon spectral finite elements and mortar elements for transient wave propagation modeling. application to ultrasonic testing of laminate composite materials, Int. J. Numer. Methods Eng. 119 (10) (2019) 964–990.

[16] O. Mesnil, A. Recoquillay, T. Druet, V. Serey, H. T. Hoang, A. Imperiale, E. Demaldent, Experimental validation of transient spectral finite element simulation tools dedicated to guided wave-based structural health monitoring, Journal of Nondestructive Evaluation, Diagnostics and Prognostics of Engineering Systems 4 (4).

[17] P. Joly, Variational Methods for Time-Dependent Wave Propagation Problems, in: Topics in Computational Wave Propagation, no. 31 in Notes Comput. Sci. Eng., Springer Berlin Heidelberg, 2003, pp. 201–264.

[18] D. Royer, E. Dieulesaint, Elastic waves in solids I: Free and guided propagation, Springer Science & Business Media, 1999.

[19] A. D. Pierce, Acoustics: an introduction to its physical principles and applications, Springer, 2019.

[20] J. M. Carcione, Wave fields in real media: Wave propagation in anisotropic, anelastic, porous and electromagnetic media, Vol. 38, Elsevier, 2007.

[21] E. Bécache, A. Ezziani, P. Joly, Mathematical and Numerical Modeling of Wave Popagation in Linear Viscoelastic Media, in: Mathematical and Numerical Aspects of Wave Propagation WAVES 2003, Springer, 2003, pp. 916–921.

[22] D. Komatitsch, J.-P. Vilotte, R. Vai, J. M. Castillo-Covarrubias, F. J. Sanchez-Sesma, The spectral element method for elastic wave equations-application to 2-D and 3-D seismic problems, Int. J. Numer. Methods Eng. 45 (9) (1999) 1139–1164.

[23] P. Joly, Numerical Methods for Elastic Wave Propagation, in: Waves in Nonlinear Pre-Stressed Materials, no. 495 in CISM Courses and Lectures, Springer Vienna, 2007, pp. 181–281.

[24] M. Durufle, P. Grob, P. Joly, Influence of Gauss and Gauss-Lobatto quadrature rules on the accuracy of a quadrilateral finite element method in the time domain, Numer. Methods Partial Differential Eq. 25 (3) (2009) 526–551.

[25] M. J. S. Chin-Joe-Kong, W. A. Mulder, M. Van Veldhuizen, Higher-order triangular and tetrahedral finite elements with mass lumping for solving the wave equation, J. Eng. Math. 35 (4) (1999) 405–426.

[26] W. A. Mulder, R. Shamasundar, Performance of continuous mass-lumped tetrahedral elements for elastic wave propagation with and without global assembly, Geophys. J. Int. 207 (1) (2016) 414–421.
[27] J. Chabassier, S. Imperiale, Stability and dispersion analysis of improved time discretization for simply supported prestressed Timoshenko systems. Application to the stiff piano string, Wave Motion 50 (3) (2013) 456–480.
[28] J. Virieux, A. Asnaashari, R. Brossier, L. Métivier, A. Ribodetti, W. Zhou, An introduction to full waveform inversion, in: Encyclopedia of exploration geophysics, Society of Exploration Geophysicists, 2017, pp. R1–1.